The Extra-Islet Pancreas Supports Autoimmunity in Human Type 1 Diabetes

Barlow, G.L.[1,2], Schürch, C.M[2,4], Bhate, S.S.[2], Phillips, D.[2], Young, A.[3,6,7], Dong, S.[3,5] Martinez, HA.[1], Kaber, G.[1], Nagy, N. [1], Ramachandran S.[1], Meng, J.[1], Korpos E.[9] Bluestone, J.A.[†,8], Nolan, G.P.[†,2], Bollyky, P.L.[†,‡,1]

† Corresponding Author
‡ Lead Contact

Affiliations:

1. Division of Infectious Diseases and Geographic Medicine, Department of Medicine, Stanford University School of Medicine, Stanford, CA 94305, USA
2. Department of Pathology, Stanford University School of Medicine, Stanford, CA 94305, USA
3. Diabetes Center, University of California San Francisco, San Francisco, CA 94143, USA
4. Department of Pathology and Neuropathology, University Hospital and Comprehensive Cancer Center, Tübingen, Germany
5. Sean N. Parker Autoimmune Research Laboratory and Diabetes Center, University of California San Francisco, San Francisco, CA, USA
6. Huntsman Cancer Institute, University of Utah Health Sciences Center, Salt Lake City, UT 84112, USA
7. Department of Pathology, University of Utah School of Medicine, Salt Lake City, UT 84112, USA
8. Sonoma Biotherapeutics, South San Francisco, CA 94080 USA
9. Institute of Physiological Chemistry and Pathobiochemistry and Cells-in-Motion Interfaculty Center, University of Muenster, Germany

Further information and requests for resources and reagents should be directed to and will be fulfilled by the lead contact, Paul Bollyky (pbollyky@stanford.edu).

Abstract

In autoimmune Type 1 diabetes (T1D), immune cells progressively infiltrate and destroy the islets of Langerhans – islands of endocrine tissue dispersed throughout the pancreas. However, it is unclear how this process, called 'insulitis', develops and progresses within this organ. Here, using highly multiplexed CO-Detection by indEXing (CODEX) tissue imaging and cadaveric pancreas samples from pre-T1D, T1D, and non-T1D donors, we examine pseudotemporal-spatial patterns of insulitis and exocrine inflammation within large pancreatic tissue sections. We identify four sub-states of insulitis characterized by $CD8^+$T cells at different stages of activation. We further find that exocrine compartments of pancreatic lobules affected by insulitis have distinct cellularity, suggesting that extra-islet factors may make particular lobules permissive to disease. Finally, we identify "staging areas" - immature tertiary lymphoid structures away from islets where $CD8^+$T cells appear to assemble before they navigate to islets. Together, these data implicate the extra-islet pancreas in autoimmune insulitis, greatly expanding the boundaries of T1D pathogenesis.

Keywords: Type 1 Diabetes; Insulitis; Autoimmunity; Multiplexed Imaging; CODEX; Systems Immunology; Tissue Architecture

Main

In Type 1 diabetes (T1D), autoimmune insulitis drives the progressive destruction of insulin-producing β-cells, resulting in a critical requirement for exogenous insulin. T1D affects over 8 million individuals world-wide with an estimated half-a-million new diagnoses each year (Gregory et al. 2022).

Recently, the first immunotherapy for delaying T1D onset teplizumab (a human anti-CD3 monoclonal antibody) was approved by the US Food and Drug Administration (FDA) (Hirsch 2023). However, this treatment and other immunotherapies only benefit some patients for reasons that are unclear (Herold et al. 2013; Perdigoto et al. 2019; Herold et al. 2019; Pescovitz et al. 2009; Orban et al. 2011; 2014; Bluestone, Buckner, and Herold 2021). A better understanding of T1D pathogenesis is essential to building on this success.

T1D pathogenesis encompasses immune infiltration of the islets, also known as 'insulitis', and inflammation of the non-islet pancreas. Insulitis has been extensively investigated and the major cell types associated with β-cell killing have been identified; however, any understanding of how the inflammation in non-islet pancreas contributes to insulitis is lacking.

One of the challenges of studying human T1D pathology is the availability of suitable tissue samples. Obtaining pancreatic biopsies raises the risk of surgical complications and the progressive nature of T1D would necessitate serial, longitudinal studies over time, which is prohibitive (Krogvold et al. 2014). Fortunately, the Juvenile Diabetes Research Foundation (JDRF) Network for Pancreatic Organ Donors with Diabetes (nPOD) have provided human pancreatic tissues from cadaveric donors for this study (Campbell-Thompson et al. 2012; Pugliese et al. 2014). nPOD has enabled substantial progress towards characterizing the cell types comprising insulitis and extra-islet inflammation (Wilcox et al. 2016; Arif et al. 2014; Leete et al. 2016; Martino et al. 2015).

The development of highly multiplexed tissue imaging technologies has empowered these efforts. Recently, Imaging Mass Cytometry (IMC) was used to uncover changes in T1D islets, including alterations in β-cell phenotypes, immune composition, vascular density, and basement membrane (Damond et al. 2019; Wang et al. 2019).

Despite these advances, our understanding of certain key features of human T1D pathology remains limited. In particular, insulitis is regulated by checkpoints that ultimately fail in T1D. However, a comprehensive and quantitative search for insulitis checkpoints has not been performed to date. Furthermore, islets in different regions of the pancreas are infiltrated at strikingly different rates for reasons that are unclear. Several lines of evidence suggest that the non-islet pancreatic tissue could be responsible by governing the targeting of islets: First, peri-insulitis, which is the accumulation of immune cells outside the islet, is observed in tissues from patients with T1D (Korpos et al. 2013), indicating that not all T cells extravasate directly into islets (Savinov et al. 2003). Second, the composition and functionality of immune and epithelial cells outside islets differ in T1D patients compared to non-diabetic controls (Rodriguez-Calvo et al. 2014; Bender et al. 2020; Campbell-Thompson et al. 2012; Campbell-Thompson, Rodriguez-Calvo, and Battaglia 2015; Fasolino et al. 2022). Finally, tertiary lymphoid structures (TLS), which are dense aggregates of lymphoid cells indicative of local immune activation, are observed

outside islets in T1D patients (Korpos et al. 2021). To date, multiplexed imaging studies have only examined islets. A comprehensive, spatially resolved cellular analysis of whole pancreatic tissue in T1D is lacking.

Here, we investigated both islet and non-islet pancreatic tissue in the progression of T1D. We applied the highly multiplexed tissue imaging platform CO-Detection by indexing (CODEX) with an antibody panel targeting 54 antigens to samples from a cohort of T1D patients with insulitis as well as non-T1D individuals with and without autoantibodies obtained through the JDRF nPOD program. We analyzed approximately 2000 islets and broad swaths of surrounding tissue to evaluate local and distal spatial architecture. We then used pseudotime analysis to characterize insulitis sub-states based on the activation states of islet-infiltrating $CD8^+$T cells. We further investigated the cellular changes in niches and lobules beyond islets. Our results implicate both the local islet microenvironment and inflammation at distal sites within the pancreas in insulitis progression, greatly expanding the boundaries of pathologic inflammation in T1D.

Cohort curation, image acquisition, and cell annotation

The JDRF nPOD is a national registry of cadaveric pancreases donated by T1D patients that has transformed the ability to investigate the pathways underlying the development and progression of human T1D (Campbell-Thompson et al. 2012; Pugliese et al. 2014). At the time of our study, 17 cases with insulitis were available from nPOD, from which we selected 10 that had visible insulitis in preliminary IHC analyses. The final cohort included two autoantibody-positive, pre-T1D cases, eight T1D cases, and three non-diabetic controls. Cases were selected by surveying the nPOD online immunohistochemistry database which contains images of tissue sections triple-stained for Insulin, Glucagon, and CD3. T1D and pre-T1D cases that had $CD3^+$ staining in islet or peri-islet spaces and tissue still available were selected for our study. The cases varied in the time between diagnosis and death from 0 years (diagnosed at death) to 6 years (Figure 1.A**,** left). The causes of death were mostly unrelated to T1D complications (Methods). Therefore, the time since diagnosis is not a reflection of the severity or aggressiveness of the individual's disease.

Large regions averaging 55 mm^2 were imaged with CODEX as previously described (Schürch et al. 2020; Phillips, Matusiak, et al. 2021; Hickey et al. 2021)**.** Regions were imaged to capture islets and the surrounding region simultaneously (Figure 1.A, center and right). The algorithm CellSeg was used to segment cell nuclei and quantify marker expression from CODEX images as previously described (Lee et al. 2022)**.** Between $3.0x10^5$ and $9.8x10^5$ cells per donor were obtained resulting in $7.0x10^6$ cells in total. Twenty-one cell types were identified with Leiden clustering and manual merging and visualized using Uniform Manifold Approximation and Projection (UMAP) (Figure 1.B). Endocrine cells were manually gated from UMAP embeddings derived from Proinsulin, Glucagon, and Somatostatin to identify β-cells, a-cells, and d-cells. Immune cells were sub-clustered with the Leiden algorithm using immune-specific markers (Figure 1.C,Supplemental Table 2). A heatmap of all cell types and their marker expression is displayed in Figure 1.D. Of note, we could not accurately identify macrophage subsets or distinguish dendritic cells from macrophages due to panel design, complex combinations of co-expression, and the difficulty in segmenting and quantifying markers on myeloid populations. Therefore, dendritic cells are contained within the 'macrophage' group for all analyses. In

addition, we identified a cell population that could not be definitively annotated, expressing high levels of CD45, CD69, Granzyme-B, and CD44, intermediate levels of CD16, S100A6, Galectin-3, and Hyaluronan, but not expressing lineage markers CD3, CD20, CD56, CD57, CD15, or MPO. We confirmed from the raw images that CD3, CD4, and CD8 were not internalized, indicating activation, nor did these cells express other T cell activation markers CD45RA, CD45RO, PD-1, or LAG-3. This population could represent a type of innate lymphoid cell or mast cells (Dalmas et al. 2017; Martino et al. 2015) and was labeled Granzyme-B$^+$/CD3- (Figure 1.D).

Islet- and non-islet regions are altered in T1D

We first sought to identify cellular changes in T1D within islets specifically. Previous reports observed that insulin-containing islets are significantly more common in recent-onset T1D cases than cases with diabetes durations of greater than one year (In't Veld 2011). Similarly, we found that samples from patients who had been diagnosed with T1D for 0-2 years had significantly reduced β-cell frequencies compared to non-diabetic controls. Lastly, samples from subjects with disease durations of 5-6 years had minimal remaining β-cell mass (Figure 1.E). Whereas one Pre-T1D case had β-cell mass comparable to those of cases with disease duration of 0-2 years, the other Pre-T1D case was comparable to non-diabetic controls (Figure 1.E).

Next, we investigated how the abundances of non-endocrine cell types inside islets differed across donors. We performed Principal Component Analysis (PCA) of the frequencies of non-endocrine cell types located in islets in each donor. Donors were clearly separated into two groups by the first two principal components; one group included all T1D cases and one pre-T1D case and the second group included all non-diabetic cases and the other pre-T1D case (Figure 1.F). In this analysis, we did not consider β-cells, α-cells, and δ-cells. Thus, donors were stratified by disease duration strictly according to the abundances of immune and other pancreatic, non-endocrine cell types in the islets.

We next considered only cells located outside islets. Again, donors were clearly separable by the first two principal components (Figure 1.G). The first principal component separated cases with times since diagnosis between 0-2 years from non-T1D, pre-T1D, and cases with diabetes durations of 5-6 years (Figure 1.G). The second principal component separated cases with diabetes durations of 5-6 years from the rest (Figure 1.G). Therefore, both the islet and non-islet spaces of T1D and non-T1D cases were distinct.

Many cell types were increased in T1D cases with times since diagnosis of 0-2 years relative to non-diabetic controls. In T1D cases with times since diagnosis of 5-6 years, the abundance of different cell types either remained higher than healthy controls or returned to baseline (Supplemental Figure 1). This trend was present in both islet and non-islet regions. These data demonstrate that the immune activity between the islet and extra-islet compartments are coordinated but the cellular programs underlying this crosstalk are unclear.

Pseudotemporal reconstruction of islet pathogenesis identifies a conserved trajectory of insulitis

In human T1D, β-cell destruction does not occur simultaneously in all pancreatic islets in an individual and even neighboring islets can be at different stages of destruction (In't Veld 2011; Damond et al. 2019). We therefore used pseudotime analysis to infer the most likely progression of a single islet through disease space (Damond et al. 2019). To develop a pseudotemporal map of the islets in our study, we quantified the cellular composition of each islet, including cells within 20 µm of the islet's boundary, and applied the pseudotime algorithm PArtition-based Graph Abstraction (PAGA) (Figure 2.A; Figure 2.B), (Wolf et al. 2019). PAGA was selected because it is a high-performing algorithm able to identify multiple trajectories, if they exist, while making minimal assumptions about the true structure (Saelens et al. 2019).

Displayed in Figure 2.B is the PAGA force-directed layout where each point represents an islet. Each islet's color corresponds to its pseudotemporal distance from the centroid of non-diabetic islets. As expected, the different donor groups (no T1D, pre-T1D, T1D) had different distributions of islets across the PAGA map (Figure 2.C). In the PAGA map, a continuum is apparent from islets abundant in insulin-expressing β-cells on the left of the map to islets depleted in β-cells on the right of the map (Figure 2.D, Figure 2.E, Figure 2.F, top row). PAGA uses Leiden clustering internally, enabling the following regions of the pseudotime map to be labelled objectively (Supplemental Figure 2.A): 1) Islets with low pseudotime values on the left of the map were labelled 'Healthy' even if they originated from T1D donors. 2) Islets in the middle of the map were elevated in HLA-ABC (MHC Class I) expression, $CD8^+$T cells, and macrophages (Figure 2.D, Figure 2.E, Figure 2.F, rows 2-4) and were labelled 'Inflamed'. 3) Islets with late pseudotime values on the right of the map were devoid of β-cells and were labelled 'β-Cell Depleted' (Figure 2.D, Figure 2.E, Figure 2.F, top row). In addition, islets lacking β-cells occasionally contained $CD8^+$T cells and were labelled 'β-Cell Depleted + Immune Islets' (Figure 2.D, Figure 2.E, Figure 2.F, rows 2-4). The presence of these islets suggests that the signals retaining $CD8^+$T cells in the islets linger after β-cell death.

Islets from non-diabetic controls and one of the pre-T1D donors (6314) were primarily in the Healthy group to the left of the map (Figure 2.C). Islets from subjects who had had T1D for of 5-6 years (cases 6195 and 6323) were primarily in the β-Cell Depleted group to the right of the map (Figure 2.C). All the remaining T1D donors and the other pre-T1D donor were distributed broadly throughout the map (Figure 2.C).

Together, these results illustrate a single, non-branching progression from Healthy Islets to β-cell depleted Islets via Inflamed Islets, consistent with previous pseudotime analyses (Damond et al. 2019).

IDO expression on islet vasculature is linked to T cell infiltration and β-cell death during insulitis

While inspecting images of islets, we occasionally observed islets with vasculature that stained positive for indoleamine 2, 3-dioxygenase 1 (IDO). In the tumor microenvironment, IDO is expressed by myeloid cells and suppresses $CD8^+$T cell activity through multiple mechanisms including induction of $FOXP3^+$ regulatory T cells and inhibition of $CD8^+$T cell proliferation (Munn and Mellor 2016). In islets, IDO was expressed by $CD31^+$ vasculature and not $CD45^+$ immune cells adjacent to vasculature (Figure 2.G). IDO was not expressed by other cell types in islets or by vascular cells outside islets (Supplemental Figure 2.B). We manually quantified vascular expression of IDO on islets throughout pseudotime and found that all but two IDO^+ islets were in the Inflamed group (Figure 2.H). Therefore, IDO expression by islet vasculature was tightly associated with inflammation.

We hypothesized that IDO expression was induced by infiltrating immune cells during insulitis. A major inducer of IDO expression is interferon-γ, a cytokine highly expressed by T cells and macrophages (Munn and Mellor 2016). We compared the frequency of $CD8^+$T cells and macrophages in islets from the Inflamed group with and without IDO^+ vasculature and found that $CD8^+$T cells were significantly more abundant in islets with IDO^+ vasculature than islets without IDO+ vasculature (Figure 2.I). The abundance of macrophages was not significantly different in the islets with and without IDO^+ vasculature (Supplemental Figure 2.C). This implies that during $CD8^+$T cell infiltration, IDO is induced on vasculature to subdue the inflammation.

Due to IDO's immunosuppressive role in the tumor microenvironment (Munn and Mellor 2016), IDO may protect β-cells from inflammation. If so, for β-cells to be eliminated, IDO-mediated suppression would need to be circumvented through its inhibition or a reduction in IDO's expression. We observed that only 3.3% of islets in the β-Cell Depleted + Immune group had IDO^+ vasculature, whereas 23.9% of islets in the Inflamed group had IDO^+ vasculature ($p = .017$ chi-square test) (Figure 2.H). This is consistent with the hypothesis that IDO expression is suppressed prior to β-cell loss.

In summary, IDO expression by islet vasculature is associated with T cell infiltration and its loss during insulitis is associated with β-cell depletion. Together, these suggest that IDO^+ vasculature is an immune regulatory checkpoint that fails in T1D.

Insulitis has sub-states, defined by functional states of $CD8^+$T cells

Insulitis is regulated by checkpoints that fail to control inflammation in T1D. For example, the islet capsule restricts $CD8^+$T cells from entering islets (Korpos et al. 2013) and PD-L1 on β-cells suppresses infiltrating $CD8^+$T cells (Osum et al. 2018). By definition, a checkpoint prevents an islet from progressing and thus can halt islets in an insulitis 'sub-state'. Cell differentiation studies have demonstrated the utility of using high-parameter data to infer checkpoints from their corresponding sub-states (Satpathy et al. 2019). We reasoned that we could identify

immunoregulatory checkpoints in T1D by identifying sub-states of insulitis. To identify insulitis sub-states, we began by characterizing the functional states of $CD8^+$T cells in islets. Although, quantifying the expression of functional markers from tissue images can be challenging due to autofluorescence, non-specific antibody staining, and signal spillover between adjacent cells, we overcame these by training a neural network to detect marker expression of single cells from raw cell-images (Figure 3.A, Supplemental Figure 3.A). Using our neural network, we quantified the expression of T cell markers on islet $CD8^+$T cells (Figure 3.B).

Overall, markers of antigen experience (PD-1, TOX, CD45RO, CD69, CD44) were the most commonly expressed on islet-infiltrating $CD8^+$T cells (Supplemental Figure 3.B). $CD8^+$T cells expressing CD45RA (which are either naïve or terminally differentiated effector memory cells) were detectable in islets, as previously reported (Damond et al. 2019) (Figure 3.B). PD-1 and TOX were commonly co-expressed on $CD45RO^+$ $CD8^+$T cells detected in islets (Figure 3.B). We also observed expression of CD69 on $CD45RO^+$ $CD8^+$T cells, which are likely tissue-resident memory cells (Kuric et al. 2017). CD69 was co-expressed with $CD45RA^+$ $CD8^+$T cells indicating that naïve T cells are being activated in islets. In addition, we observed a rare population of $CD45RO^+$ $CD8^+$T cells that co-expressed multiple functional markers including CD69, CD44, LAG-3, Granzyme-B, and ICOS (Figure 3.B bottom clade). Lastly, a rare population of $CD57^+$ $CD8^+$T cells was present but these cells rarely co-expressed LAG-3, Granzyme-B, or ICOS (Figure 3.B top clade). These populations bear a resemblance to the two exhausted T cell populations identified in the peripheral blood of T1D patients that were associated with responsiveness to alefacept (Diggins et al. 2021). The heterogeneous functional states of $CD8^+$T cells in islets demonstrate varying stages of activation, suggesting that they receive additional stimulation after reaching islets.

We expected that insulitis sub-states would be characterized by specific combinations of $CD8^+$T cell states found in islets together. To interrogate this, we performed UMAP only on Inflamed islets, using the frequencies of $CD8^+$T cells expressing each functional marker. Leiden clustering identified four inflamed sub-clusters, I-IV, (Figure 3.C top). Here, the term “sub-cluster” is used to highlight that these groups were all contained within the previously defined “Inflamed” cluster and the roman numerals are expressly not intended to imply a temporal ordering. Inflamed–I contained only $CD8^+$T cells that did not express any of the functional markers analyzed (Figure 3.C bottom, top row). Inflamed–II was characterized by a high frequency of $CD45RA^+CD8^+$T cells (Figure 3.C bottom, second row from top and Figure 3.D top row). Inflamed–III was characterized by a low frequency of $CD45RA^+$ cells and high frequency of $CD45RO^+$ and $PD\text{-}1^+$ cells that did not co-express any functional markers (Figure 3.C bottom, third row from top and Figure 3.D middle row). Inflamed–IV was characterized by an enrichment of $CD8^+$T cells expressing CD57 or LAG-3, ICOS, and Granzyme-B in addition to PD-1 and CD45RO Inflamed–III (Figure 3.C bottom, bottom row and Figure 3.D bottom row). In summary, the diversity of $CD8^+$T cells in any particular islet is much more restricted than the diversity of total islet $CD8^+$T cell states.

The fact that the inflamed sub-clusters are characterized by $CD8^+$T cells at different stages of activation suggests that the inflamed sub-clusters represent different stages of a progression rather than distinct trajectories (either within or across patients). In support of this, each individual donor possessed islets that belonged to more than one inflamed islet sub-cluster (Figure 3.E). Therefore, Inflamed–I through Inflamed–IV do not represent patient subtypes but insulitis sub-states conserved among T1D patients.

Regulation of insulitis sub-states by the islet microenvironment

To identify cellular or molecular factors that regulate the state of CD8$^+$T cells in islets, we first asked if CD8$^+$T cell states are enriched in islets or extend into the peri-islet and exocrine space. To this end, we computed the frequencies of each CD8$^+$T cell state inside the islet and in separate swaths of 0-25µm, 25-50µm and 50-100µm away from the islets (Supplemental Figure 3.C). We found that for islets of Inflamed-II, -III, and -IV, functional markers characterizing the CD8$^+$T cells were expressed more frequently inside islets than in the surrounding tissue areas. This demonstrated that differences in the compositions of CD8$^+$T cell states in different islets were due to the islet microenvironment and not the surrounding exocrine spaces.

Although macrophages are abundant in islets from the Inflamed group (Figure 2.E,Figure 2.F) and are capable of interacting with T cells through antigen presentation and cytokine secretion, neither the expression of markers of macrophage activity nor macrophage abundance was significantly associated with islets from inflamed sub-clusters (Supplemental Figure 3.D). Similarly, no other cell-type nor the vascular expression of IDO was linked to CD8$^+$T cell programs in islets (Supplemental Figure 3.D). These negative data suggest that transitions between insulitis states are independent of changes in the abundance of any of the cell types identified in our tissues. Consistent with this, the four inflamed sub-clusters had identical distributions throughout the original PAGA force-directed layout (Figure 3.F). These data suggest that insulitis sub-states are transient over the course of insulitis and the CD8$^+$T cell states are being regulated by highly dynamic processes.

Lastly, β-cells are likely to influence the state of T cells within islets. We reasoned that islets lacking β-cells but containing immune cells could provide information regarding the role of β-cells in regulating the CD8$^+$T cell compartment. We therefore examined CD8$^+$T cells in islets from the β-cell Depleted + Immune group relative to those in islets from the Inflamed group. We found that TOX was expressed by a higher frequency of CD8$^+$T cells in β-Cell Depleted + Immune islets than CD8$^+$T cells in Inflamed islets (Figure 3.G), indicating that TOX$^-$ CD45RO$^+$ T cells are either short lived or exit upon loss of β-cells. In addition, CD45RA was enriched in CD8$^+$T cells in β-cell Depleted + Immune islets and that CD45RO was depleted (Figure 3.G). This suggests that CD45RA$^+$ CD8$^+$T cells convert to CD45RO$^+$ in islets and that β-cells are necessary for this process. If this model is correct, CD45RA$^+$ CD8$^+$T cells in Inflamed islets are specific for islet antigens and are not inert bystanders. Together, these data indicate that islet CD8$^+$T cells are stimulated upon entering islets and the factors that regulate this process are highly dynamic (Figure 3.H).

Vasculature, nerves, and Granzyme-B$^+$/CD3- cells outside islets are associated with the lobular patterning of islet pathogenesis

The destruction of islets in T1D is known to exhibit lobular patterning (Gepts 1965). Specifically, islets in the same lobule are likely to be in the same stage of disease. This architecture suggests

that the states of islets within the same lobule are coordinated but the cell types responsible are unknown. To systematically investigate lobular patterning in T1D, we used a neural network to segment lobules and assign each single cell to its lobule. We used the intra-class correlation coefficient (ICC) to quantify the variation in islet pseudotime within a lobule relative to variation in islet pseudotime donor wide. ICC ranges from 0 to 1 with cases closer to 1 having a stronger lobular effect on islet pseudotime (Figure 4.A). Islets of non-T1D cases and 6314, 6195, and 6323 did not have appreciable variability in their pseudotimes, so the ICC was not applicable, but in the remaining cases, the ICCs ranged from 0.17 to 0.74 (Figure 4.B). This highlights that the magnitude of lobular patterning ranges widely across T1D cases with insulitis and thus could be influenced by donor characteristics such as the time since diagnosis, etiology or genetics.

To identify cell types that coordinate the behavior of islets within lobules, we employed hierarchical linear modeling (HLM), a statistical framework designed to identify relationships between different levels of multi-level data. HLMs are standard in many fields where multi-level data are common (Gelman et al. 2014.) and have been applied in biomedical settings (Jerby-Arnon and Regev 2022; Yi et al. 2019). We were interested in cell-types if their abundance per lobule correlated with the average islet pseudotime per lobule. Importantly, we omitted cells located in islets from the calculation of a cell type's lobular abundance so that information from the pseudotime analysis would not leak into this analysis. For each cell type, we estimated the effect of its total abundance in a lobule (the number of cells divided by the number of acinar cells to normalize for lobule area) on the pseudotimes of islets in that lobule. We performed this analysis in two-level HLMs for each donor and a three-level HLM considering all donors together.

We then examined cell types that were significantly associated with lobules across multiple T1D tissue donors. The abundance of three cell types were associated with pseudotime in more than two cases. These were vasculature, Granzyme-B$^+$/CD3- cells, and nerves, all of which were more abundant in lobules with islets late in pseudotime (Figure 4.C boxed rows, Figure 4.D). Samples from cases 6323 and 6195 which had very few insulin-containing islets, had increased abundances of vasculature, Granzyme-B/CD3- cells, and nerves (Supplemental Figure 1), indicating these changes persist at least until the entire tissue is afflicted. In addition, vasculature, Granzyme-B$^+$/CD3- cells, and nerves were increased in Inflamed islets compared to Healthy islets indicating that they may serve a role in islets in addition to their role in the non-islet compartment (Supplemental Figure 4). It was noteworthy that the conventional pathogenic immune cells comprising insulitis were not associated with lobular patterning. For example, CD8$^+$T cells and macrophages were only significant in one donor, and CD4$^+$T cells and B cells were significant in only two donors (Figure 4.C). Therefore, they may depend on detecting signals from vasculature, Granzyme-B$^+$/CD3- cells, and nerves in the extra-islet tissue to target a given lobule and the islets therein.

Immature tertiary lymphoid structures far from islets are enriched in subjects with T1D

We hypothesized that pancreatic niches may influence the extravasation, migration, or activation of T cells prior to them reaching islets. To characterize pancreatic niches that might influence

CD8$^+$T cells, we identified Cellular Neighborhoods (CNs) in the pancreas (Schürch et al. 2020; Bhate et al. 2021). CNs are tissue regions that are homogeneous and have defined cell-type compositions. To identify CNs, briefly, single cells were clustered according to the cell-type composition of their twenty nearest spatial neighbors and automatically annotated with the names of enriched cell types (Figure 5.A, See Methods). This resulted in 75 CNs.

Next, we identified CNs that were more abundant in T1D than non-T1D tissues (Figure 5.B). The top three CNs (fold change of abundance in T1D relative to abundance in non-T1D) were (CD8$^+$T cells|B Cells), (Macrophage|Stromal Cells|B Cells), and (Vasculature|B Cells). All were rich with B cells (Figure 5.B, Figure 5.C). We asked whether these three CNs were commonly adjacent to each other this could indicate that they act as components of a larger structure playing a functional role in the tissue (Bhate et al. 2021). Measuring the adjacency of the three B cell CNs demonstrated that the (CD8$^+$T cells|B Cells) CN is predominantly found adjacent to both the other CNs but that (Macrophage|Stroma|B Cells) and (Vasculature|B Cells) are less commonly adjacent to each other (Figure 5.D).

We next asked whether these CN assemblies corresponded to either peri-vascular cuffs (Agrawal et al. 2013; Wekerle 2017) or tertiary lymphoid structures (TLSs) (Korpos et al. 2021; Rovituso et al. 2016; Agrawal et al. 2013), as these are two lymphoid-rich structures commonly present in autoimmune conditions. Although the (CD8$^+$T cells|B Cells) CN was adjacent to vessels (Figure 5.D, Figure 5.E), it was not in the fluid-filled perivascular space, as is the case with perivascular cuffs (Figure 5.E). In our samples, the (CD8$^+$T cells|B Cells) CN did not have segregated T cell and B cell zones as seen in mature TLSs, but the size, abundance, and association with vasculature was comparable with those previously described of TLSs in human T1D (Korpos et al. 2021).

In summary, the (CD8$^+$T cells|B Cells) CN is more abundant in T1D tissues that are undergoing active inflammation than in non-T1D tissues as well as in tissues of patients who had T1D for more than 4 years. Finally, this CN shares many architectural features of immature TLSs.

Immature tertiary lymphoid structures are potential staging areas for islet-destined CD8$^+$T cells

We next asked whether the (CD8$^+$T cells|B Cells) CN had high endothelial venules (HEV), specialized blood vessels that enable naïve lymphocytes to extravasate into peripheral tissues, which are commonly found in TLSs. We observed expression of peripheral lymph node addressin (PNAd), an HEV marker, in the vessels associated with the (CD8$^+$T cells|B Cells) CN (Figure 5.E left image) but not in other vessels (data not shown). Although we could not assess the presence of other TLS traits such as follicular dendritic cells, fibroblastic reticular cells, or follicular helper T cells, the cellular composition and presence of HEVs indicate that instances of the (CD8$^+$T cells|B Cells) CN represent immature TLSs.

Next, we asked if immature TLSs were supporting the entry of naïve CD8$^+$T cells into the pancreas. We observed CD8$^+$T cells co-expressing CD45RA and CD62L (the ligand for PNAd) near PNAd$^+$ vasculature (Figure 5.E, middle and right image respectively). Thus, naïve CD8$^+$T cells in the pancreas can adhere to HEV receptors. Furthermore, CD45RA$^+$ was enriched three-fold on CD8$^+$T cells in the (CD8$^+$T cells|B Cells) CN relative to CD8$^+$T cells in the tissue as a whole (Figure 5.F),

providing additional evidence that naïve T cells enter the pancreas through HEVs in the (CD8$^+$T cells|B Cells) CN.

To determine if immature TLSs delivered naïve lymphocytes directly to islets or acted as "staging areas" by depositing them far from islets, we quantified the frequency of TLSs adjacent to islets. We found that instances of the (CD8$^+$T cells|B Cells) CN both adjacent (Figure 5.G.1) or not adjacent (Figure 5.G.2) to islets. Quantifying this adjacency frequency revealed that fewer than half were adjacent to islets (Figure 5.H). We reasoned that even if TLSs were far from islets, extravasating cells may migrate to islets from TLSs. Accordingly, islet-adjacent CD45RA$^+$ CD8$^+$T cells (that were not in islet-adjacent TLSs) co-expressed CD62L, suggesting that they originated from the (CD8$^+$T cells|B Cell) CN (Figure 5.I). Consistent with this, in one notable tissue donor, regions of the pancreas with β-cell depleted islets were enriched in the (CD8$^+$T cells|B Cell) CN relative to regions of the pancreas with β-cell containing islets (Figure 5.J). This spatial correlation between the (CD8$^+$T cells|B Cells) CN and the destruction of islets implicates the CN directly with islet pathology even when it is not adjacent to islets (Figure 5.J). Therefore, our data indicate that immature TLSs act as staging areas by enabling naïve CD8$^+$T cells to enter the pancreas far from islets where they then traffic to islets.

Discussion

We have performed a comprehensive, pseudotemporal analysis of whole pancreatic tissue in T1D using CODEX imaging of cadaveric pancreatic tissues from T1D subjects and computational approaches. Our data support several conclusions.

First, a conserved trajectory of insulitis is present across individual donors and stages of T1D progression. This trajectory is comprised of four sub-states of insulitis each characterized by CD8$^+$T cells at different stages of activation. Moreover, they indicate that T cells receive additional stimulation after entering islets. Multiple inflamed sub-clusters were represented in all T1D donors, indicating that the sub-clusters reflect sub-states capable of inter-converting rather than distinct trajectories of insulitis that stratify patients.

In addition, we observed that IDO+ vasculature was present in inflamed islets with higher frequencies of CD8$^+$T cells but rare in islets that have lost insulin and contain immune cells, suggesting that IDO is a tolerogenic checkpoint that is lost prior to β-cell death. Leveraging this checkpoint to protect transplanted β-cells from rejection has shown promise (Alexander et al. 2002) and could be combined with similar approaches using programmed death-ligand 1 (Yoshihara et al. 2020; Castro-Gutierrez et al. 2021).

These data support a model wherein all islets in all T1D cases pass through a series of insulitis substages – perhaps corresponding to immunoregulatory checkpoints - before β-cells are destroyed. This model extends the one previously suggested by Damond et al, who proposed a single trajectory for insulitis (Damond et al. 2019).

Second, pancreatic lobules affected by insulitis are characterized by distinct tissue markers. We discovered that lobules enriched in β-cell-depleted islets were also enriched in nerves, vasculature, and Granzyme-B$^+$/CD3- cells, suggesting these factors may make particular lobules permissive to disease. This could be through recruiting immune cells selectively into islets of

particular lobules. Alternatively, the infiltration of a small number of islets in an otherwise unaffected lobule could be a rate-limiting step after which the exocrine space promotes fast dissemination of pathogenic immune cells within the lobule. The role of islet enervation in T1D has been studied but such work has focused on nerves in the islet rather than nerves throughout the lobule (Christoffersson, Ratliff, and von Herrath 2020). It is noteworthy that the cell types linked with direct islet invasion were distinct from those linked to lobule targeting even though both sets of cell types were found across islet and non-islet regions. Therefore, for insulitis to consume every islet, crosstalk may be required between the cell types of both compartments. Conversely, inhibiting this interaction might contain pathology to isolated lesions.

Finally, we identify “staging areas” - immature tertiary lymphoid structures away from islets where $CD8^+$T cells assemble, most likely before they navigate to islets Our pseudotime analysis data suggest naïve $CD8^+$T cells can enter the pancreas within these “staging areas” before migrating to islets. Similar structures were observed in mice where blocking immune egress from lymph nodes led to a contraction in the size of TLSs and halted diabetes (Penaranda et al. 2010). Thus, therapeutic targeting of immune cell trafficking to TLS could mitigate sustained autoimmunity against β-cells in human T1D.

Together, these data implicate both the local islet microenvironment and inflammation at distal sites within the pancreas in insulitis progression. Our findings expand both the anatomical and cellular scope of autoimmunity in T1D.

A major limitation for the study is the cohort size. Cases with documented insulitis are very rare, significantly limiting the feasibility of curating large cohorts. While we did examine over 2,000 individual islets and included both non-diabetic and pre-diabetic controls, larger studies with more diverse patient donor cohorts are needed.

Another limitation is our limited perspective on myeloid cell populations. Although antibodies in our panel detect numerous myeloid markers, we failed to identify any heterogeneity in myeloid populations during insulitis. This was likely due in part to the difficulty of segmenting myeloid cells and quantifying marker expression due to their morphology. Combining spatial or non-spatial transcriptomics could be used in future studies to better define the myeloid populations and extend the CODEX panel.

Lastly, our samples are 2-dimensional sections which could affect some of the adjacency relations.

In conclusion, using a data-driven approach, we mapped conserved sub-states of insulitis to infer regulatory checkpoints that fail in T1D and integrated the spatial pathology of islet and non-islet regions into a single model of T1D pathogenesis. The tools and computational pipelines developed here will enable further investigation of immune pathology at the tissue scale that may lead to development of therapies for T1D.

Methods

Human tissues

Cadaveric pancreatic FFPE tissue sections were obtained through the nPOD program, sponsored by the Juvenile Diabetes Research Fund. Case numbers cited herein are assigned by nPOD and comparable across nPOD-supported projects. 17 cases in the nPOD biorepository had been previously documented to possess insulitis. For each of these 17 cases, we examined the triple stained IHC images (CD3, Insulin, and Glucagon) using nPOD's online pathology database to select blocks in which insulitis was present. To ensure that the tissue regions still contained insulitis (and had not been sectioned extensively since their images were uploaded to the nPOD pathology database), we re-sectioned and visualized CD3, Insulin, and Glucagon. We then selected 2 cases at different stages of disease (as defined by time since diabetes diagnosis). 3 non-diabetic age matched cases were selected as negative controls. The use of cadaveric human tissue samples is approved by Stanford University's Institutional Review Board.

CODEX data collection

CODEX Antibody Generation and Validation. Oligonucleotides were conjugated to purified, carrier-free, commercially available antibodies as previously described (Schürch et al. 2020; Kennedy-Darling et al. 2021). For validation experiments, human tonsil and pancreas tissues were co-embedded in a new FFPE blocks so both tissues could be stained and imaged simultaneously. Each antibody in the CODEX panel was validated by co-staining with previously established antibodies targeting positive and negative control cell-types. Once validated, the concentration and imaging exposure time of each antibody were optimized. The tissue staining patterning was compared to the online database, The Human Protein Atlas, and the published literature. The specificity, sensitivity, and reproducibility of CODEX staining has been previously validated (Schürch et al. 2020; Kennedy-Darling et al. 2021; Black et al. 2021; Phillips, Schürch, et al. 2021; Phillips, Matusiak, et al. 2021)

CODEX Staining. Staining and imaging was conducted as previously described (Schürch et al. 2020; Kennedy-Darling et al. 2021; Phillips, Schürch, et al. 2021; Black et al. 2021). Briefly, FFPE tissues were deparaffinized and rehydrated. Heat-induced epitope retrieval (HIER) antigen retrieval was conducted in Tris/EDTA buffer at pH9 (Dako) at 97°C for 10 minutes. Tissues were blocked for 1 hour with rat and mouse Ig, salmon-sperm DNA, and a mixture of the non-fluorescent DNA oligo sequences used as CODEX barcodes. Tissues were stained with the antibody cocktail in a sealed humidity chamber overnight at 4°C with shaking. The next day, tissues were washed, fixed with 1.6% paraformaldehyde, 100% methanol, and BS3 (Thermo Fisher Scientific), and mounted to a custom-made acrylic plate attached to the microscope.

CODEX Imaging. Imaging was conducted using the Keyence BZ-X710 fluorescence microscope with a CFI Plan Apo λ 20x/0.75 objective (Nikon). "High resolution" mode was selected in Keyence Navigator software, resulting in a final resolution of .37744 µm/pixel. The exposure times are listed in Supplemental Table 3. Regions for imaging were selected by rendering HLA-ABC, Proinsulin, and CD8 and selecting multiple bounding boxes to maximize the amount of tissue

imaged and minimize imaging of empty coverslip. Depending on the tissue shape and islet distribution, each donor was imaged across 2-7 regions ranging from 5x5 to 10x 3mm per region. The full antibody panel and cycle-ordering is detailed in (Supplemental Tables 3 and 4). Biotinylated hyaluronan-binding protein was rendered by adding streptavidin-PE at 1:500 concentration to the 96 well plate containing fluorescent oligos in the last cycle and running the CODEX program normally. DRAQ5 was added to the last cycle because we found it stained nuclei more evenly than HOECHST which slightly improved segmentation. Tissues took between 3 and 7 days to image depending on the tissue area.

Image Pre-processing. Drift compensation, deconvolution, z-plane selection was performed using the CODEX Toolkit uploader (github.com/nolanlab/CODEX, Goltsev et al. 2018). Cell segmentation using the DRAQ5 nuclear channel and lateral bleed compensation was performed with CellSeg (Lee et al. 2022).

Cell Type Clustering and Annotation

Marker expression was z-normalized within each donor and subsequently clustered in two steps. First, cells were projected into 2 dimensions using the 'Tissue markers' indicated in Supplemental Table 2 and Parametric Uniform Manifold Approximation and Projection (pUMAP)(Sainburg, McInnes, and Gentner 2021) was applied on a downsampled dataset. The fit model was used to transform the remaining cells. Cell types were gated using Leiden clustering and manual merging. The cluster containing immune cells was sub-clustered using the 'Immune Markers' detailed in Supplemental Table 2. Acinar cells contaminating the Immune cluster were gated out and merged with the Acinar cluster from the previous step. The Endocrine class was sub-clustered into α-, β-, and δ-Cells using Glucagon, Proinsulin, and Somatostatin respectively. Clusters were annotated according the heatmap marker expression.

Islet Segmentation and Pseudotime

Preprocessing. Windows consisting of the twenty nearest spatial neighbors surrounding each single cell were clustered according to their cell-type composition using Mini Batch K Means with k=200. For this analysis, α-, β-, and δ-Cells were combined into one 'Endocrine' cell type. One cluster was highly enriched in Endocrine cells and accurately defined the islet area. Individual islets were identified using the connected components algorithm and filtering out islets that had fewer than ten total cells. For each islet, the number of each cell type inside the islet and between the islet edge and 20μm beyond were extracted. To adjust for variation due to the islet size, the cell type counts were divided by the number of endocrine cells inside the islet. Data were then log-transformed.

PAGA Analysis. The PAGA embedding was computed using the default parameters except for the following: The neighborhood search was performed using cosine distance and 15 nearest neighbors; Leiden clustering used a resolution of 1. For computing the pseudotime values (used in the colormap in Figure 2B, the x-axis in Figure 2F, and Figure 4), the path through the inflamed islet was isolated by temporarily omitting 25 islets positioned in the middle of the map between Healthy and β-cell depleted islets. Only 9 of these were from T1D or pre-T1D donors.

Quantification and Validation of Functional Marker Gating

Annotation of Ground-Truth Dataset. 3963 $CD8^+$T cells were labelled for fifteen markers by an immunologist familiar with the staining patterns of each marker using VGG Image annotator (Abhishek Dutta and Andrew Zisserman 2019).

Automated Thresholding. For each functional marker of interest, the lateral-bleed-compensated mean fluorescence (Lee et al. 2022) of background cells were used to calculate a background distribution. Background cells were cells except those assigned to cell types that were known to express the markers of interest or autofluorescence. Marker-positive cells were defined as those whose expression was greater than the 99^{th} percentile of the background distribution.

Gating with Neural Network: Cell images were split into training, validation, and test splits (60/ 15/25). The ResNet50 architecture and initial weights were imported from the Keras library pre trained on ImageNet. Image augmentation consisted of random flips, rotations, zooms, contrast, and translation (+/- ten pixels only). All weights were unfrozen, and the model was trained for 100 epochs (see attached source code for training details).

Sub-clustering of Inflamed Islets with Cell-Type specific Functional Markers

For each Inflamed Islet (n=351), the frequency of each marker expressed by $CD8^+$T cells was computed. Single cells inside the islet and within 20µm from the islet's edge were combined before the frequency was measured. The subsequent matrix underwent z-normalization followed by UMAP and clustering using Bokeh. β-Cell Depleted + Immune Islets were defined as islets without β-cells with greater than two $CD8^+$T cells and greater than seven macrophages. These thresholds correspond to the 95^{th} percentiles of $CD8^+$T cells and macrophages in Healthy islets.

Identification of Cellular Neighborhoods

Previously, CNs (Schürch et al. 2020) were identified by, for each single cell, defining its 'window' as the 20 spatial nearest neighbors. Cells were clustered according to the number of each cell type in their windows using Mini Batch K-Means. The output clusters corresponded to CNs. To ensure our method was sensitive to rare neighborhoods, we adapted this algorithm by intentionally over-clustering, using k=200 in the K- Means step rather than using a k ranging from 10-20 as used elsewhere (Bhate et al. 2021; Phillips, Matusiak, et al. 2021; Shekarian et al. 2022). Next, to determine which cell types were characteristic of each cluster, we identified, for each cluster, the set of cell-types that were present in more than 80% of the windows allocated to that cluster. We named the clusters according to this set of cell-types and merged all clusters with the same name, resulting in seventy-five CNs. Acinar cells and epithelial cells were used in the kNN graph and in the clustering but were not considered when merging clusters. Note that this method does not differentiate neighborhoods that have the same combination of cell types but different stoichiometries.

Lobule Segmentation

A training dataset was generated by manually tracing the edges of lobules in ImageJ using the ROI function. The ROI were then floodfilled in Python and used as masks for training. For each tile, the blank cycle was selected to distinguish tissue from background coverslip. A U-Net model was trained for 10 epochs (see attached source code for training details). After stitching together all masks, the resulting images required slight refinement where lobules were not completely separated, and this was done manually in ImageJ. The connected components in the stitched image defined the lobule instances. Cells were assigned to a lobule by indexing the lobule mask with their X and Y coordinates. Cells in the inter-lobular space were assigned to one "edge" lobule. This resulted in 464 lobules.

Formulation of Hierarchical Linear Models

For each lobule, the number of each cell type in non-islet cells was divided by the number of acinar cells in the lobule. For all HLMs, the lme4 package for R was used (Bates et al. 2015) and statistical significance was computed using the lmerTest package for R (Kuznetsova, Brockhoff, and Christensen 2017). Lobular cell-type abundance was z-normalized within each donor and the pseudotime was z-normalized across the entire dataset prior to fitting. For each cell type, a two-level, random intercept HLM within each donor was constructed with the following formulation (in R formula syntax): $pseudotime_{islet} \sim celltype_{lobule} + (1|loduleID)$ and a three-level random intercept, random slope HLM including islets from all donors was formulated: $pseudotime_{islet} \sim celltype_{lobule} + (1+celltype_{lobule}|donorID) + (1|loduleID)$. Here, $pseudotime_{islet}$ equals the pseudotime of each islet, $celltype_{lobule}$ equals the number of the given cell type in a particular lobule divided by the number of acinar cells in that lobule, z-normalized within each donor, and *loduleID* and *donorID* are categorical variables specifying the lobule and donor that the given islet belongs to.

Neighborhood Adjacency

The adjacency between neighborhoods was computed as in (Bhate et al. 2021). The only modification was that neighborhood instances were identified using connected components of the k-NN graph with k=5 rather than from the thresholded images.

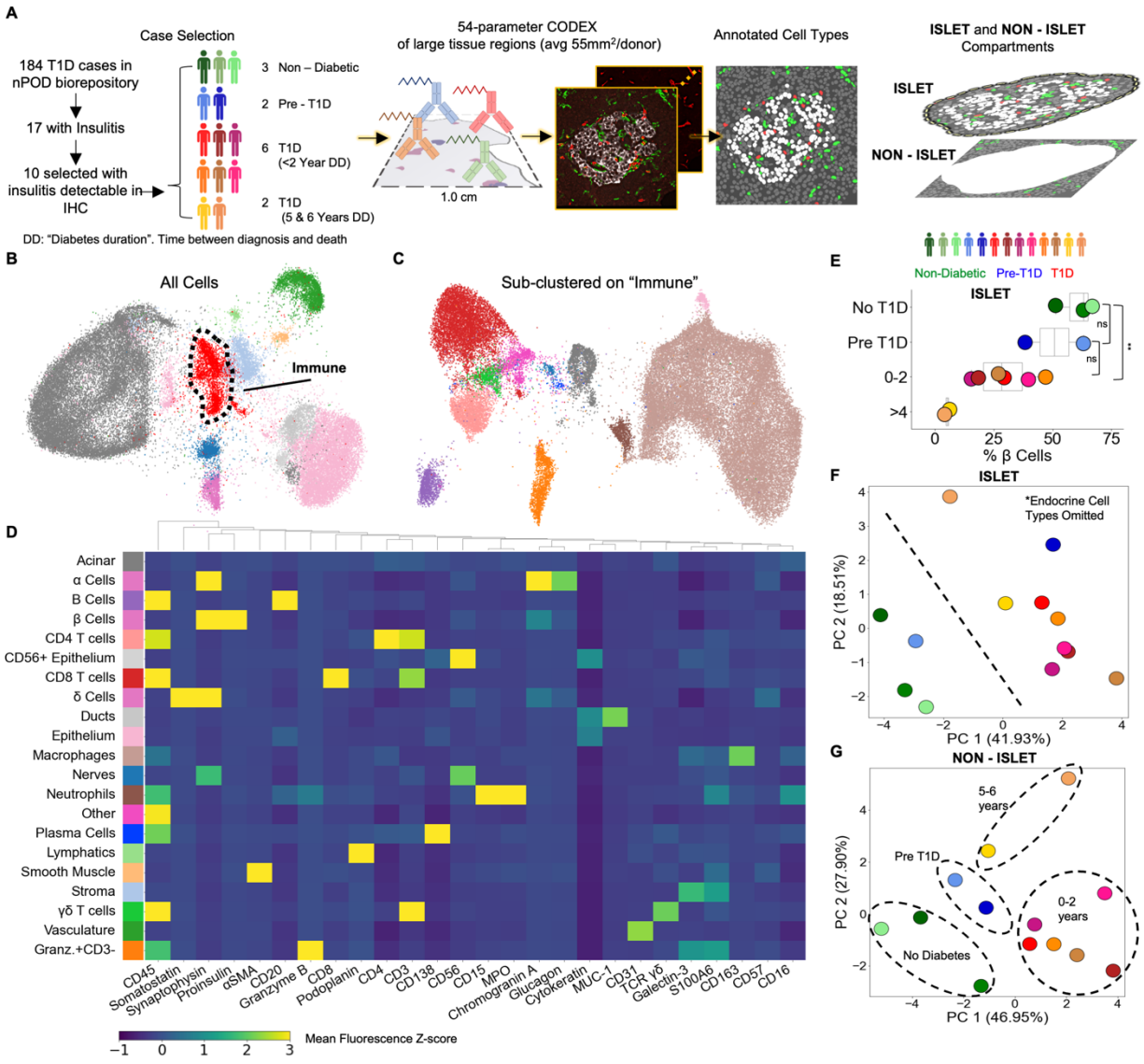

Figure 1 Profiling of T1D pancreata with CODEX high-parameter imaging reveals alterations in islet and non-islet regions.

Figure 1.A Left: Schematic of the workflow for selection of nPOD cases. Blues, greens, and reds indicate non-diabetic, pre-T1D, or T1D status, respectively. Center: Schematic for acquisition and processing of CODEX highly multiplexed imaging dataset. Right: Schematic of islet and non-islet pancreatic regions.

Figure 1.B UMAP and Leiden clustering of major cell types. Colors match those in heatmap shown in Figure 1D, except for the immune cluster, which is shown in red.

Figure 1.C UMAP of immune cluster further clustered from the immune population identified in Figure 1B. Colors match those in heatmap shown in Figure 1D.

Figure 1.D Heatmap of mean z-normalized marker expression in each cell-type cluster (color-coded on the left). Only a subset of the markers used for the UMAP are included in the heatmap to facilitate visualization. A full description of the markers used for the clustering stages is available in Supplemental Table 2.

Figure 1.E Frequency of β-Cells per donor determined by dividing the number of β-cells by the total number of β-cells, α-cells, and δ-Cells. Blues, greens, and reds indicate non-diabetic, pre-T1D, or T1D status, respectively. Significance was determined using the t-test (* $p<0.05$, ** $p<0.01$, *** $p<0.001$)

Figure 1.F Principal component analysis of islet compartment. The number of cells of each cell type (omitting α-, β-, and δ-cells) were divided by the number of endocrine cells to adjust for different islet areas. Blues, greens, and reds indicate non-diabetic, pre-T1D, or T1D status, respectively.

Figure 1.G Principal component analysis of non-islet compartment. The number of cells of each cell type (omitting α-, β-, and δ-cells) were divided by the number of acinar cells to adjust for different areas imaged. Blues, greens, and reds indicate non-diabetic, pre-T1D, or T1D status, respectively.

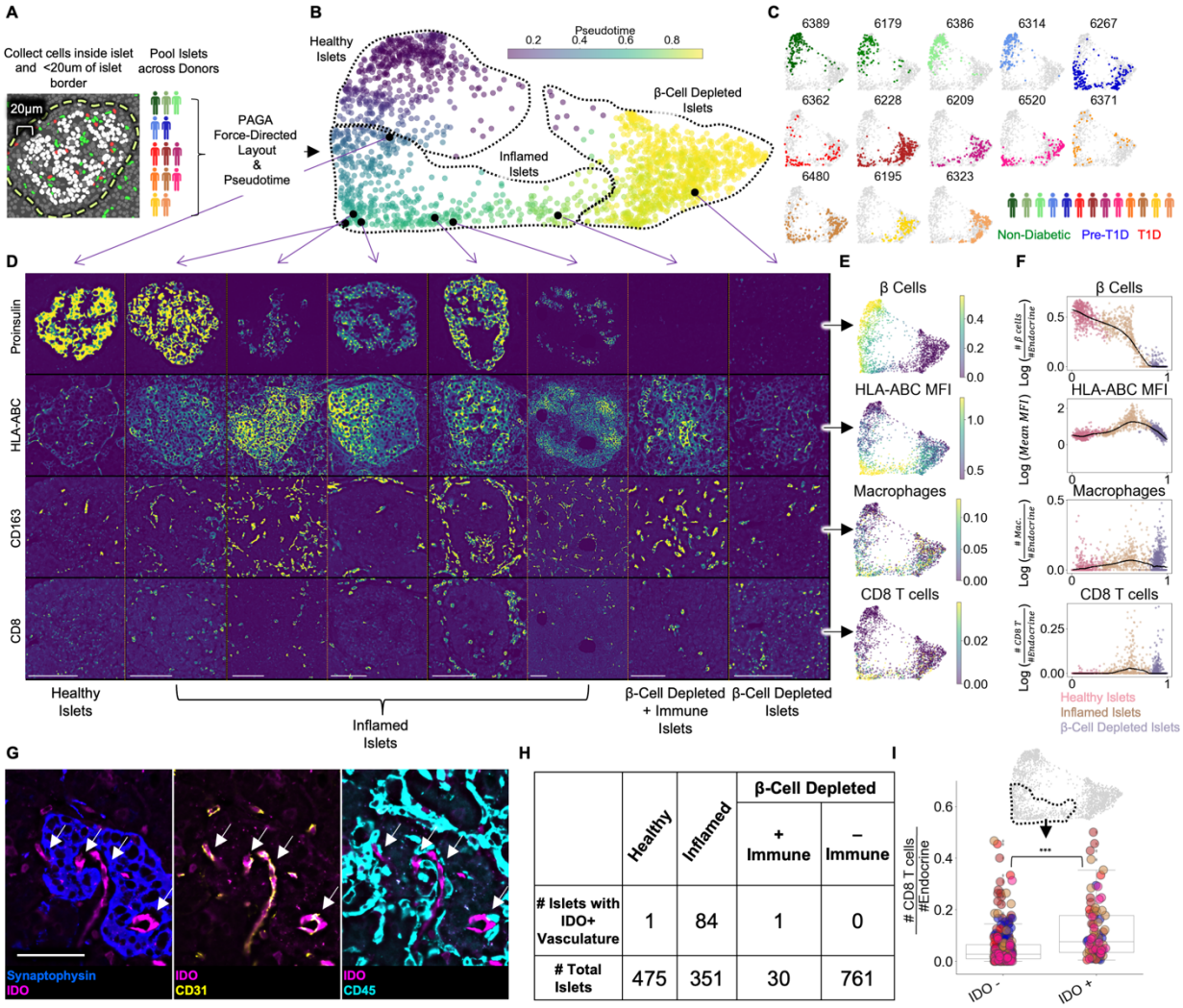

	Healthy	Inflamed	β-Cell Depleted	
			+ Immune	– Immune
# Islets with IDO+ Vasculature	1	84	1	0
# Total Islets	475	351	30	761

Figure 2 Pseudotemporal reconstruction of insulitis identifies IDO on islet vasculature as a regulatory checkpoint.

Figure 2.A Schematic of islet segmentation and quantification of islet cellular composition.

Figure 2.B PAGA-force directed layout of islets colored by pseudotime. The start point of pseudotime was calculated as the centroid of the non-diabetic islets. Representative islets from different stages of pseudotime are indicated with black points and their raw images are depicted in Figure 2.D Healthy, Inflamed, and β-Cell Depleted were identified by examining the cell composition of the clusters obtained internally by the PAGA algorithm (Supplemental Figure 2.A).

Figure 2.C Islet distribution across pseudotime for each donor. The titles indicate nPOD case IDs as in Supplemental Table 1.

Figure 2.D Images of Proinsulin, HLA-ABC, CD163, and CD8 staining in islets representative of different points along pseudotime as indicated in B. Scale bars (lower left of each column) indicate 100µm.

Figure 2.E Quantification of selected features across pseudotime overlaid onto the PAGA force-directed layout. For β-cells, macrophages, and $CD8^+$T cells, the values correspond to log(# cells/# endocrine cells). For HLA-ABC, the mean HLA-ABC expression for each cell in the islet was computed and log transformed.

Figure 2.F Quantification of selected features across pseudotime. For β-cells, macrophages, and $CD8^+$T cells, the values correspond to log(# cells/# endocrine cells). For HLA-ABC, the mean HLA-ABC expression for each cell in the islet was computed and log transformed. Color legend: Healthy islets: pink; Inflamed islets: brown; β-Cell Depleted islets: purple. Black points demarcate LOWESS regression.

Figure 2.G Representative image of an islet from the Inflamed group stained with IDO and, from left to right, Synaptophysin, CD31, and CD45. Arrows indicate $IDO^+/CD31^+$ vasculature. Right shows that IDO^+ cells are negative for CD45and therefore, are not myeloid cells associated with vasculature. Scale bar (bottom left image) indicates 50 µm.

Figure 2.H Distribution of IDO expression on islet vasculature across pseudotime.

Figure 2.I Association of IDO^+ islet vasculature with islet $CD8^+$T cell density. The y-axis corresponds to the number of $CD8^+$T cells per endocrine cell per islet. $CD8^+$T cell counts were normalized to adjust for islet size. The x-axis indicates islets whether islets contain IDO^+ vasculature. Each color corresponds to a donor. All donors with detectable IDO^+ Islet vasculature are displayed which consisted of 6480, 6267, 6520, 6228, and 6362. Colors are same as in Figure 2.C. IDO^+ vasculature was manually quantified. For combined donors, significance was determined with a mixed-effect linear model, $p = 1.5 \times 10^{-12}$ (Satterthwaites's method lmerTest R package).

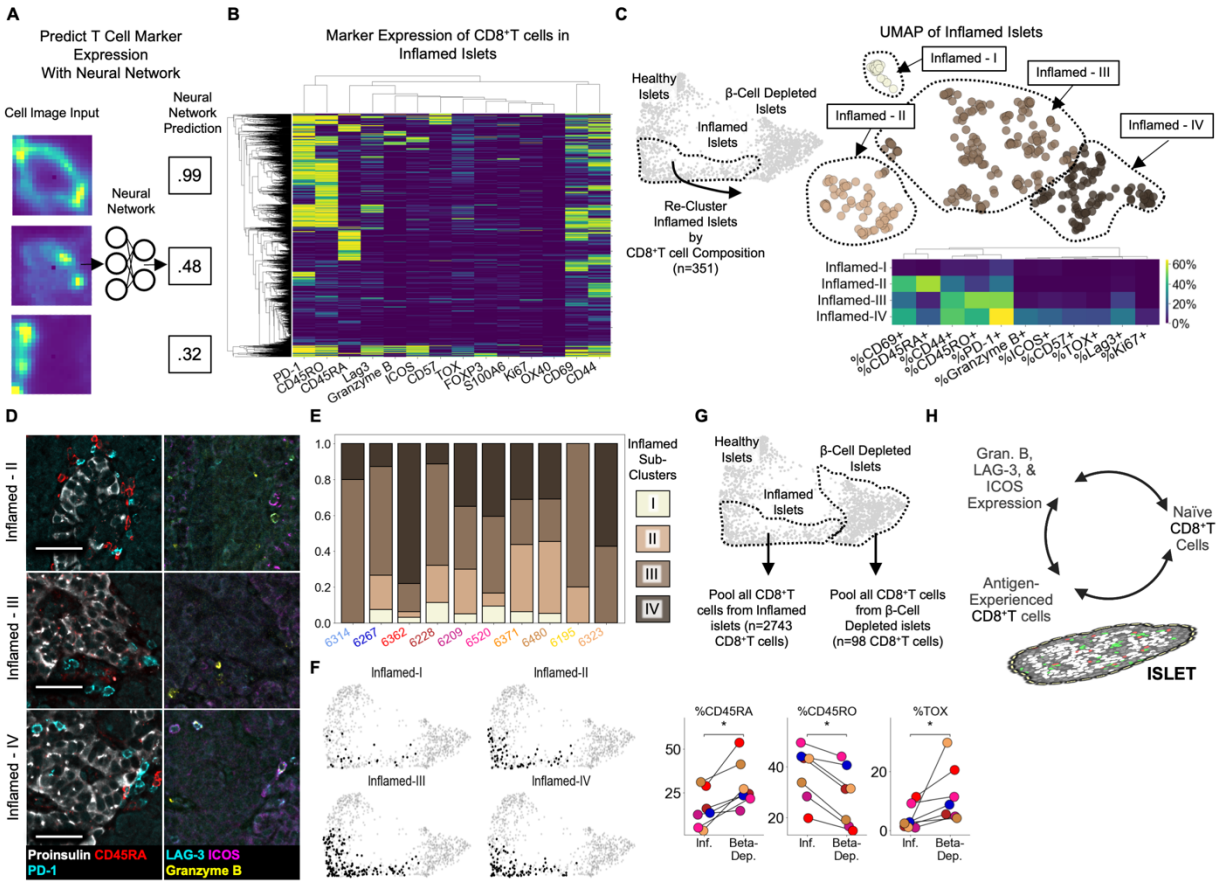

Figure 3 Insulitis has sub-states, characterized by CD8⁺T cell functionality

Figure 3.A Schematic of marker-quantification with a ResNet50 neural network. Raw images are input, and the neural network outputs a number between 0 and 1 indicative of the level of confidence that the cell expresses that marker with 1 indicating the highest confidence.

Figure 3.B Heatmap of all 2,855 Inflamed Islet CD8⁺T cells, hierarchically clustered according to marker expression predicted by the neural network.

Figure 3.C Top) UMAP of Inflamed Islets based on frequencies of markers on CD8⁺T cells in islets. Bottom) Mean frequencies of each marker on CD8⁺T cells in islets of each inflamed sub-cluster.

Figure 3.D Representative images of islets from each subcluster with associated immune markers. Scale bars indicate 50 µm.

Figure 3.E Frequencies of islets from each subcluster per donor in pre-T1D and T1D samples. Color indicates subcluster as in panel C.

Figure 3.F Distribution of the islets of Inflamed-I through -IV on the PAGA force-directed layout shown in Figure 2.B

Figure 3.G Differences in marker expression frequencies between CD8⁺T cells in islets from the Inflamed group and from the β-Cell Depleted + Immune group. T cells from all islets of the

specified groups were pooled within each donor to compute the frequencies of marker expression. Significance was determined using the Wilcoxon signed-rank test (* p<0.05, ** p<0.01, *** p<0.001) and was not corrected for multiple hypothesis testing.

Figure 3.H Proposed model of coordinated T cell states in islets due to stimulation and re-stimulation of CD8⁺T cells in islets.

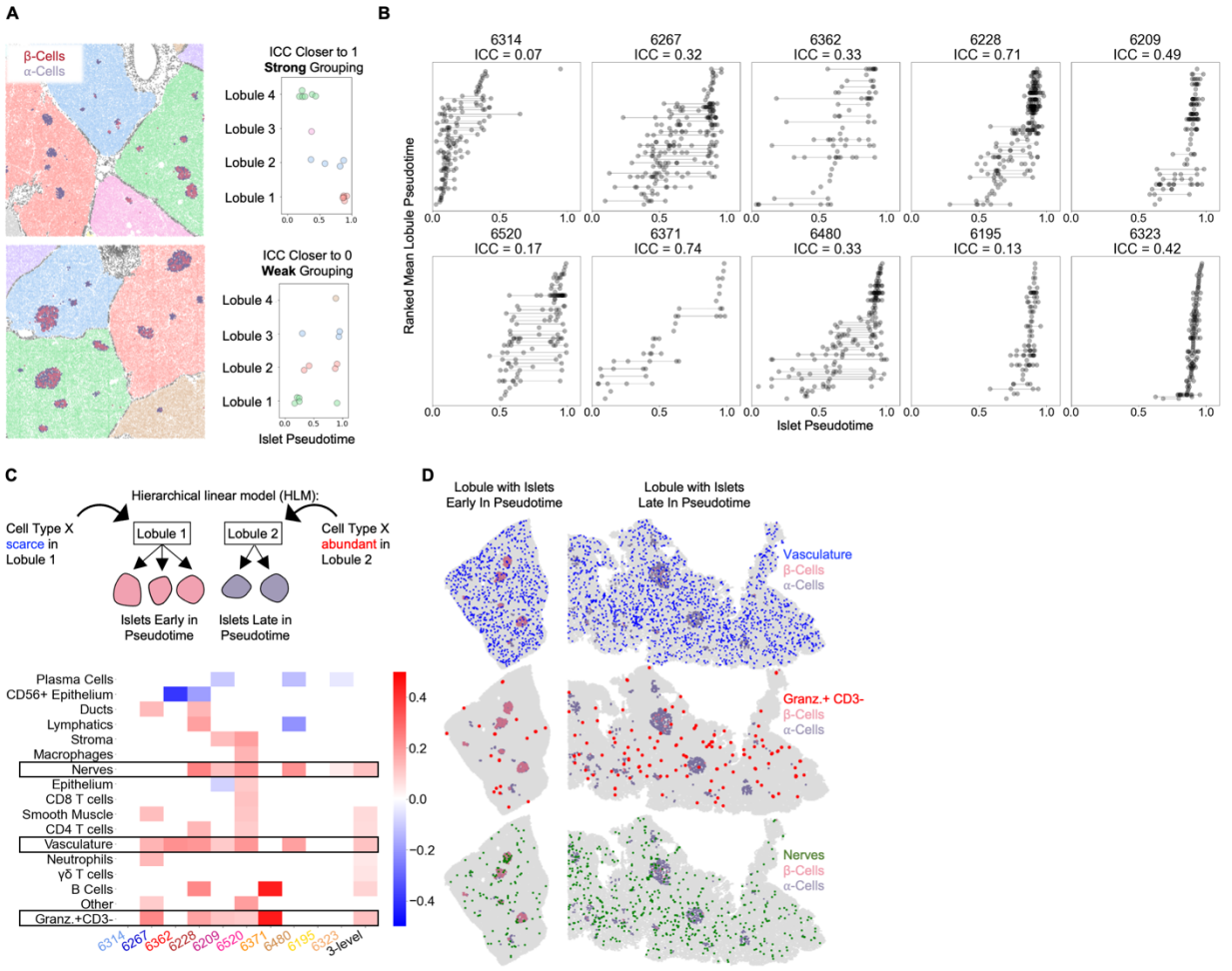

Figure 4 Vasculature, nerves, and Granzyme-B⁺/CD3- cells outside islets are associated with the lobular patterning of islet pathogenesis

Figure 4.A A schematic of the method for quantifying lobular patterning of insulitis. Lobules were segmented and individual islets were mapped back to the lobules where they were found. Top: An example region with a strong lobular grouping effect and an ICC closer to 1. Bottom: An example region with a weak lobular grouping effect and an ICC closer to 0.

Figure 4.B Islet pseudotimes in each nPOD donor with pre-T1D or T1D grouped by lobule. Each point represents an islet. The x-axis represents the islet pseudotime. The y-axis represents each lobule ranked by the mean pseudotime of islets in that lobule. Violin plots per lobule are overlaid. Abbreviations: ICC: Intraclass correlation coefficient.

Figure 4.C Cell types associated with lobular patterning. Top: Schematic of the hierarchical linear model. Cells in islets were omitted when computing the lobular abundance of each cell-type. Bottom: Coefficients of two-level models trained on each donor separately (columns labeled by donor) and a three-level model (right column). Color corresponds to the coefficient and features with p>0.05 are white. Significance was determined using Satterthwaites's method in the lmerTest R package. No adjustment for multiple hypothesis testing was applied.

Figure 4.D Visualization of vasculature (top), Granzyme-B/CD3- cells (middle), and nerves (bottom) in two lobules. The left lobule represents lobules with islets earlier in pseudotime and a lower abundance of the given cell type in the lobule. The right lobule represents lobules with islets late in pseudotime and a greater abundance of the given cell type in the lobule.

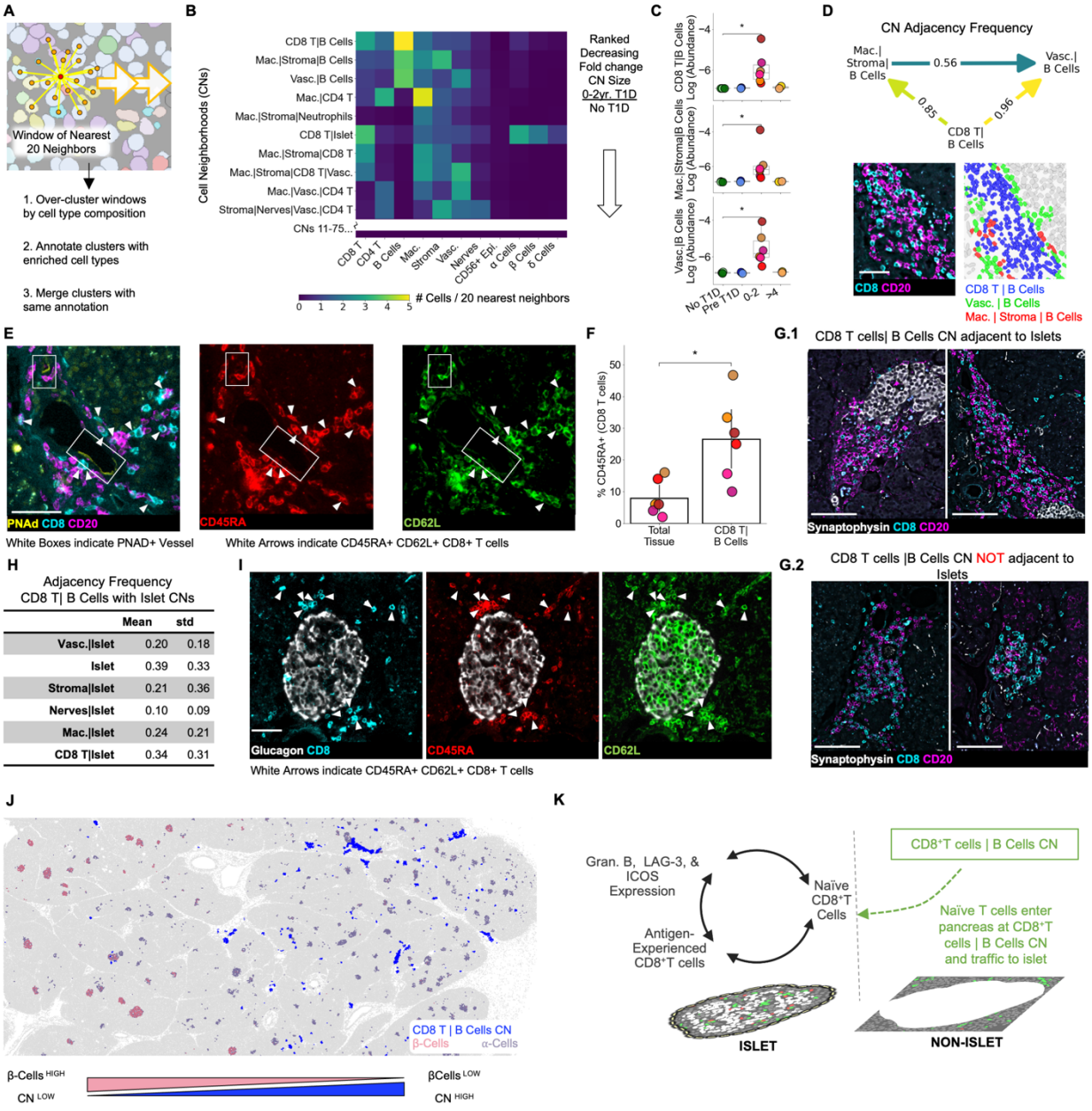

Figure 5 Immature tertiary lymphoid structures far from islets are potential staging areas for islet-destined CD8⁺T cells

Figure 5.A Schematic of algorithm for identifying CNs. Red point indicates index cell for the CN. Orange points indicate the nearest neighbors of the index cell. Windows are collected for each cell in the dataset (indicated by orange arrows).

Figure 5.B Cell-type compositions of the top CNs organized in decreasing order of the fold increase in abundance in T1D vs. non-T1D samples. Each column in the heatmap indicates the mean density of that cell type in the 20 nearest spatial neighbors of cells assigned to the CN designated for that row. Abundance was calculated as the number of cells assigned to the given CN divided by the number of acinar cells. Abbreviations: Vasc.: vasculature; Mac.: macrophages; Lym.: lymphatics. Neu.: neutrophils; CD8 T: CD8⁺T cells; CD4 T: CD4⁺T cells. Endocrine cell types were merged during CN annotation and are labeled “Islet”.

Figure 5.C Mean abundances of the CD8⁺T cell and B cell CNs per donor. Abundance was calculated as the number of cells assigned to the given CN divided by the number of acinar cells. Significance was determined using the Mann-Whitney U test (* $p<0.05$,** $p<0.01$, *** $p<0.001$). No adjustment for multiple hypothesis testing was applied.

Figure 5.D Top: Adjacency frequencies of (CD8⁺T cells| B Cell CN) with (Macrophage|Stroma|B Cells) and (Vasculature| B Cells) CNs. The adjacency frequency was calculated as the number of instances of the source CN adjacent to the destination CN divided by the total number of instances of the source CN. Bottom Left: Raw image of a representative assembly of the three CNs (CD8⁺T cells| B Cell CN), (Macrophage|Stroma|B Cells), and (Vasculature| B Cells) displaying CD8 and CD20 staining. Bottom Right: The same assembly as to the left colored by CN. Scale bar indicates 50µm).

Figure 5.E Representative images of co-localization of PNAd⁺ endothelium and CD45RA⁺ CD62L⁺ CD8⁺T cells located in the (CD8⁺T cells|B Cells) CN. Scale bar indicates 50µm.

Figure 5.F Enrichment of CD45RA expression on CD8⁺T cells located in (CD8⁺T cell | B cell) CN relative to CD8⁺T cells throughout the tissue. Significance was determined with a Wilcoxon signed-rank test (* $p<0.05$, ** $p<0.01$, *** $p<0.001$).

Figure 5.G Representative images in case 6209 of (CD8⁺T cells|B Cells) instances adjacent to islets (G.1) and not adjacent to islets (G.2). Scale bars indicate 200µm.

Figure 5.H Quantification of the adjacency frequencies between the (CD8⁺T cells|B Cells) CN and CNs rich in endocrine cells (i.e “Islet CNs”). Mean, std: mean and standard deviation adjacency frequency across T1D donors. Abbreviations: Vasc.: vasculature; Mac.: macrophage.

Figure 5.I Representative images in case 6209 of islet-associated CD45RA⁺ CD62L⁺ CD8+T cells. Scale bar indicates 50 µm.

Figure 5.J Image in case 6209 showing the spatial distribution of the (CD8⁺T cells|B cells) CN instances relative to islets and the enrichment of (CD8⁺T cells|B cells) CN instances in areas of the pancreas with islets lacking β-Cells.

788 Figure 5.K Proposed model of coordinated T cell stimulation in islets in T1D rejuvenated by naïve
789 T cells that enter the pancreas at the ($CD8^+$T cells|B Cells) CN outside islets.

790
791

792
793

794

Supplemental Information

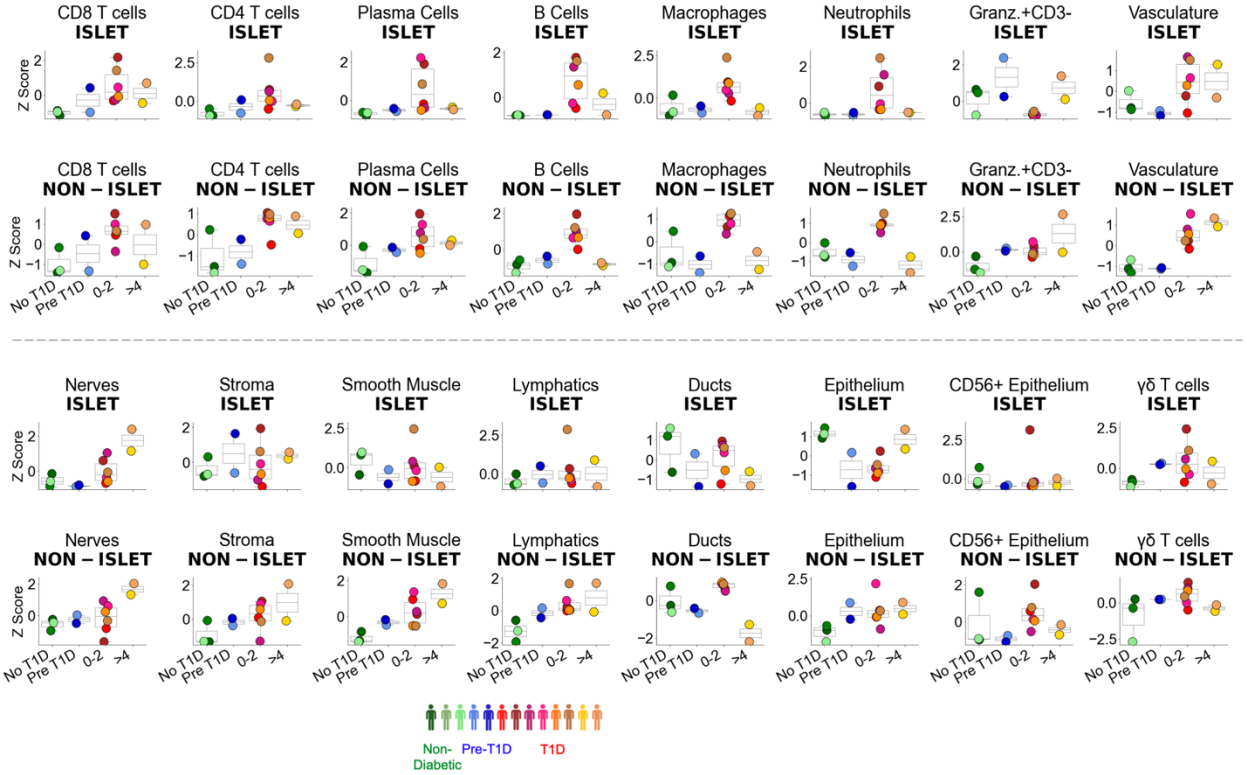

Supplemental Figure 1 **Related to Figure 1.**

Supplemental Figure 1.A Changes in cellular abundance in Islet (top) and non-islet (bottom) regions. The Y-axis corresponds to the number of the given cell type / number of endocrine cells in the top row and the number of a given cell type / number of acinar cells in the bottom row in each donor. These frequencies were then z-normalized across donors.

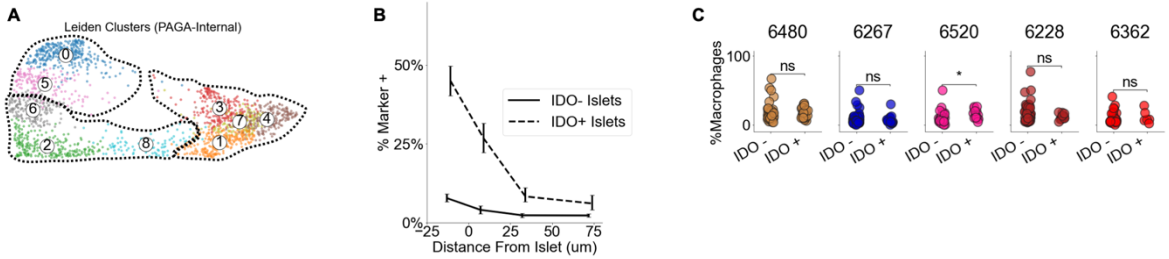

Supplemental Figure 2 **Related to Figure 2.**

Supplemental Figure 2.A Leiden clustering computed by PAGA algorithm internally. Clusters 0 and 5 were assigned to the 'Healthy' group. Clusters 6, 2, and 8 were assigned to the "Inflamed" group. Clusters 1,3,7, and 4 were assigned to the "β-Cell Depleted" group.

Supplemental Figure 2.B Frequency of IDO on vasculature at different distances from islets. Dashed line indicates the frequency in and around islets where IDO$^+$ was detected in islet vasculature (n=84) as in Figure 2.H. Solid line indicates the frequency in and around Inflamed Islets in which IDO was absent (n=267). Error bars indicate 95% confidence intervals obtained by iteratively calculating the marker frequency in re-sampled islets with replacement (n=200)

Supplemental Figure 2.C Macrophage abundance in IDO$^+$ and IDO$^-$ islets. Same as Figure 2.I. Asterisks in figure indicate significance within each donor. For combined donors, significance was determined with a mixed-effect linear model, p = 0.72 (Satterthwaites's method lmerTest R package).

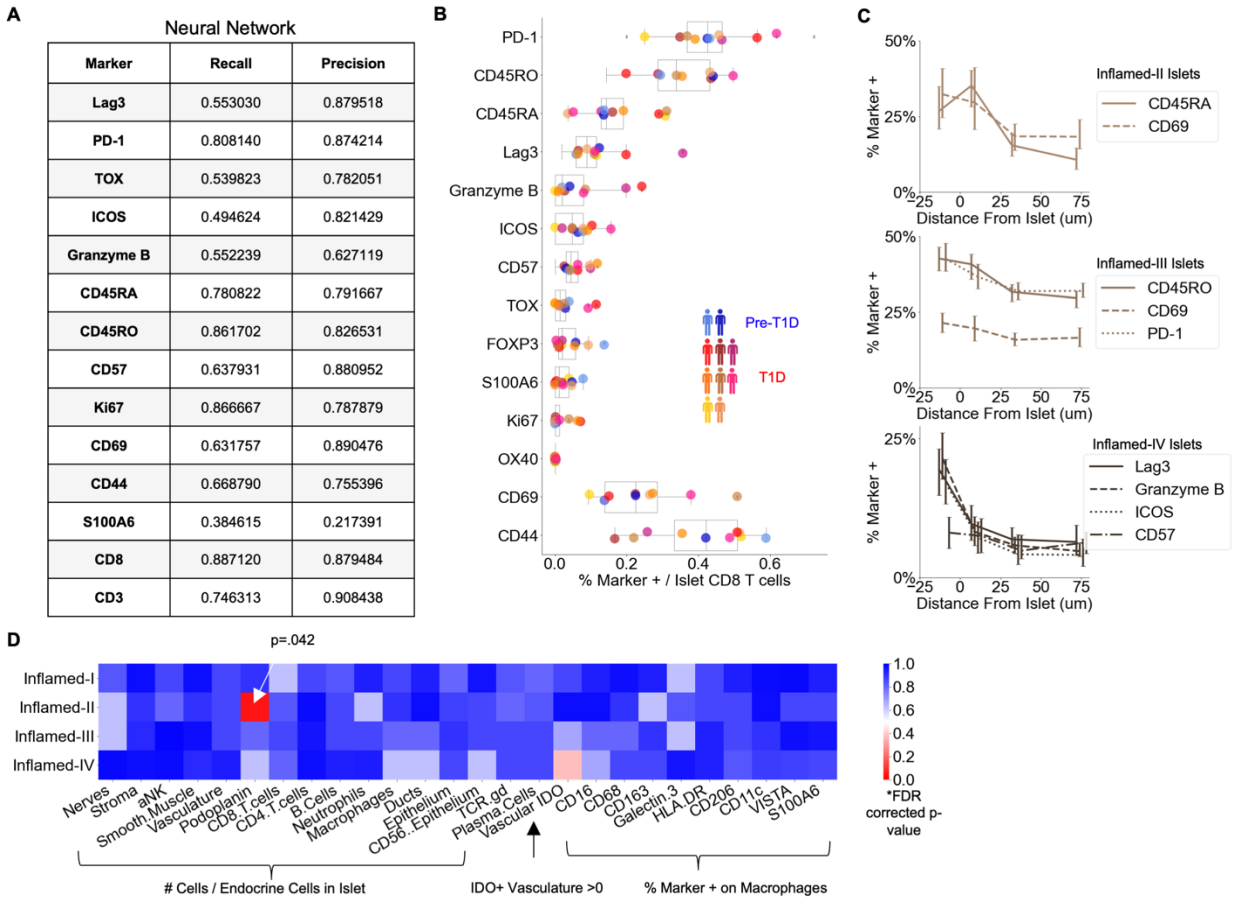

Supplemental Figure 3 Related to Figure 3

Supplemental Figure 3.A Validation of neural network for detecting expression of weak antigens. Left: Recall and Precision for the automated gating scheme (see Methods). Right: Recall and Precision for the neural network. Both tables were computed using cells in the "Test" dataset unseen by the neural network.

Marker	Recall	Precision
Lag3	0.553030	0.879518
PD-1	0.808140	0.874214
TOX	0.539823	0.782051
ICOS	0.494624	0.821429
Granzyme B	0.552239	0.627119
CD45RA	0.780822	0.791667
CD45RO	0.861702	0.826531
CD57	0.637931	0.880952
Ki67	0.866667	0.787879
CD69	0.631757	0.890476
CD44	0.668790	0.755396
S100A6	0.384615	0.217391
CD8	0.887120	0.879484
CD3	0.746313	0.908438

Supplemental Figure 3.B Frequency of functional markers on CD8$^+$T cells inside islets. Colors correspond to donor. Only Pre-T1D and T1D donors are displayed.

Supplemental Figure 3.C Frequency of functional markers on CD8^{+}T cells at different distances from islets. Error bars indicate 95% confidence intervals obtained by iteratively calculating the marker frequency in re-sampled islets with replacement (n=200).

Supplemental Figure 3.D Association of islet features with Inflamed-I through -IV. For each feature (columns), a mixed-level model adjusting for donor was fit in a one-vs-all design and the p-value was determined using Satterthwaites's method in lmerTest R package. Values in the heatmap were corrected for multiple hypotheses using the Benjamini, Hochberg method.

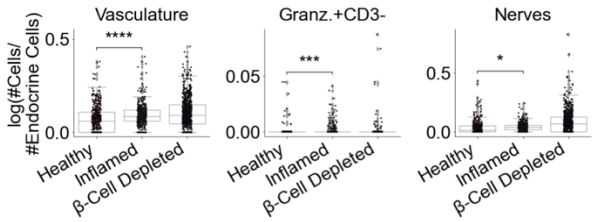

Supplemental Figure 4 Related to Figure 4

Supplemental Figure 4.A Changes in cell types identified by HLM in insulitis. Each point represents and islet. Islets are grouped according to the pseudotime analysis from Figure 2. The y-axis corresponds to the log-transformed values for the number of the given cell type / number of endocrine cells. Significance was determined using the t-test (* p<0.05,** p<0.01, *** p<0.001). No adjustment for multiple hypothesis testing was applied.

CaseID	Donor Type	Age (years)	Diabetes Duration (years)	Cause of Death	Sex	Ethnicity	BMI	nPOD RRID
6267	Autoab positive	23	NA	Anoxia	Female	Caucasian	16.59	SAMN15879321
6314	Autoab positive	21	NA	Head Trauma	Male	Caucasian	23.8	SAMN15879368
6520	T1D	21.61	0	Cerebrovascular/	Male	Caucasian	29.3	SAMN18053203
6362	T1D	24.9	0	Head Trauma	Male	Caucasian	28.5	SAMN15879415
6228	T1D	13	0	Anoxia	Male	Caucasian	17.4	SAMN15879284
6209	T1D	5	0.25	Cerebral edema secondary to DKA	Female	Caucasian	15.9	SAMN15879265
6371	T1D	12.5	2	Cerebral edema	Female	Caucasian	16.6	SAMN15879424
6480	T1D	17.18	2	DKA	Male	Caucasian	27.1	SAMN15879533
6195	T1D	19.3	5	Head Trauma	Male	Caucasian	23.7	SAMN15879251
6323	T1D	22	6	Anoxia	Female	Caucasian	24.7	SAMN15879377
6389	No diabetes	18.6	NA	Head Trauma	Male	Caucasian	20.9	SAMN15879442
6179	No diabetes	20	NA	Head Trauma	Female	Caucasian	20.7	SAMN15879235
6386	No diabetes	14	NA	Head Trauma	Male	Caucasian	23.9	SAMN15879439

Supplemental Table 1: **nPOD Case Information**

Both	"All" UMAP	"Immune" UMAP	Endocrine Cells	Un-used ****
Channel 2 Blank*	alphaSMA	VISTA	Glucagon	CD44
Channel 3 Blank*	Synaptophysin	TCR g/d	Insulin	CD45RA
Channel 4 Blank*	Podoplanin	MPO	Proinsulin	CD45RO
S100A6	PD-L1 ***	HLA-DR	Somatostatin	CollIV
Hoechst**	NaKATPase	FOXP3		HABP
Granzyme B	MUC-1	CD8		HLA-ABC
Galectin-3	Draq 5	CD69		ICOS
CD68	Cytokeratin	CD4		IDO
CD57	Chromogranin A	CD206		Ki67
CD56	CD31	CD16		Lag3
CD45		CD11c		OX40
CD3		BCL-2		PD-1
CD20				TOX
CD163				
CD15				
CD138				

Supplemental Table 2: **Markers used for cell-type identification.** Channels in the "Both" column were used for clustering all cells and specifying immune cells. Channels in the "All" column were only used for clustering all cells and the UMAP in Figure 1.B. Channels in "Immune" columns were only used for sub-clustering immune cells and the UMAP in Figure 1.C. Channels in "Endocrine" column were used for sub-clustering endocrine populations. Channels in "Un-used" column were not included in the clustering or UMAP step because they were either too weak to aid clustering or were expressed on multiple cell-populations and confounded cell-type identification.

	AntiBody	A488	ExposuresTime	AntiBody	A555	ExposuresTime	AntiBody	A647	ExposuresTime
Cycle 1	CollIV	33	333	NaKATPase	36	100	HLA-ABC	53	100
Cycle 2	blank	blank	1000	blank	blank	1000	blank	blank	1000
Cycle 3	Ki67	6	100	BCL-2	46	500	TOX	28	150
Cycle 4	Chromogranin A	43	16	empty		1	FOXP3	61	1000
Cycle 5	Proinsulin	63	40	Galectin-3	60	166	empty		1
Cycle 6	Glucagon	24	50	Podoplanin	32	500	Insulin	30	200
Cycle 7	CD8	8	125	CD31	68	100	Lag3	42	500
Cycle 8	CD15	14	40	CD45RA	7	333	PD-1	23	500
Cycle 9	MPO	51	117	CD69	52	500	PD-L1	11	500
Cycle 10	S100A6	70	500	empty		1	CD3	77	500
Cycle 11	MUC-1	21	33	CD20	48	167	CD4	20	500
Cycle 12	Cytokeratin	67	100	CD16	15	250	CD11c	49	500
Cycle 13	alphaSma	69	50	CD163	45	100	empty		1
Cycle 14	CD57	57	300	Somatostatin	2	100	CD56	29	333
Cycle 15	CD44	44	250	CD206	55	400	CD45RO	3	500
Cycle 16	TCR g/d	72	1000	CD45	56	250	ICOS	41	500
Cycle 17	empty		1	Synaptophysin	26	250	Granzyme B	81	100
Cycle 18	empty		1	HLA-DR	65	250	OX40	66	400
Cycle 19	empty		1	VISTA	79	500	CD138	76	200
Cycle 20	empty		1	IDO	59	2500	CD68	5	100
Cycle 21	empty		1	HABP	1/100 StrPE	13	Draq 5		115

Supplemental Table 3: CODEX Experiment Details

Marker	Clone	Vendor	Identifier
ColIIV	poly	Abcam	ab6586
Ki67	B56	BD	556003
Chromogranin A	.K2H10 + PHE5 + CGA/41	Novus	NBP2-34674
Proinsulin	3A1	Thermo	MA122710
Glucagon	K7bB10	Abcam	ab10988
CD8	C8/144B	Santa Cruz	sc-53212
CD15	MMA	BD	559045
MPO	poly	R&D	AF3667
S100A6	7D11	Novus	NB100-1765
MUC-1	955	NSJ Bioreagents	V2372SAF
Cytokeratin	C11	Biolegend	628602
alphaSma	polyclonal	abcam	ab5694
CD57	HCD57	Biolegend	359602
CD44	IM-7	Biolegend	103002
TCR g/d	H-41	Santa Cruz	sc-100289
NaKATPase	EP1845Y	Abcam	ab167390
BCL-2	124	Cell Marque	custom
Galectin-3	A3A12	Thermo	MA1940
Podoplanin	NC-08	Biolegend	916606
CD31	C31.3 + C31.7 + C31.10	Novus Bio	NBP2-47785
CD45RA	HI100	Biolegend	555486
CD69	poly (AF2359)	Novus	AF2359
CD20	rIGEL/773	Novus	NBP2-54591
CD16	D1N9L	CST	custom
CD163	EDHu-1	Novus	NB110-40686
Somatostatin	7G5	Novus	NBP2-37447
CD206	poly	R&D	AF2534
CD45	2B11 + PD7/26	Novus	NBP2-34528
Synaptophysin	7H12	Novus	NBP1-47483
HLA-DR	EPR3692	abcam	ab215985
VISTA	D1L2G	CST	custom
IDO	D5J4E	CST	custom
biotinylated Hyaluronan Binding Protein (HABP)	Bollyky Lab Stanford University		custom
HLA-ABC	EMR8-5	BD	565292
TOX	E6I3Q	CST	custom
FOXP3	236A/E7	Invitrogen	14-4777-80
Insulin	K36AC10	Sigma	SAB4200691
Lag3	D2G4O	CST	custom
PD-1	D4W2J	CST	custom
PD-L1	E1L3N	CST	custom
CD3	D7A6E	CST	custom
CD4	EPR6855	Abcam	ab181724
CD11c	EP1347Y	AbCam	ab216655
CD56	MRQ-42	Cell Marque	custom
CD45RO	UCH-L1	Santa Cruz	sc-1183
ICOS	D1K2T	CST	custom
Granzyme B	EPR20129-217	Abcam	ab219803
OX40	Ber-ACT35	Biolegend	Ber-ACT35
CD138	B-A38	Invitrogen	MA1-10091
CD68	D4B9C	CST	916104
PNAD	MECA-79	Biolegend	120801
CD62L	B-8	SCBT	QT 48070

Supplemental Table 4: **Antibody Clone Details**

References

Abhishek Dutta and Andrew Zisserman. 2019. "The VIA Annotation Software for Images, Audio and Video." In . MM '19. Nice, France: ACM. https://doi.org/10.1145/3343031.3350535.

Agrawal, Smriti M., Jacqueline Williamson, Ritu Sharma, Hania Kebir, Kamala Patel, Alexandre Prat, and V. Wee Yong. 2013. "Extracellular Matrix Metalloproteinase Inducer Shows Active Perivascular Cuffs in Multiple Sclerosis." *Brain* 136 (6): 1760–77. https://doi.org/10.1093/brain/awt093.

Alexander, Angela M., Megan Crawford, Suzanne Bertera, William A. Rudert, Osamu Takikawa, Paul D. Robbins, and Massimo Trucco. 2002. "Indoleamine 2,3-Dioxygenase Expression in Transplanted NOD Islets Prolongs Graft Survival After Adoptive Transfer of Diabetogenic Splenocytes:" *Diabetes* 51 (2): 356–65. https://doi.org/10.2337/diabetes.51.2.356.

Arif, Sefina, Pia Leete, Vy Nguyen, Katherine Marks, Nurhanani Mohamed Nor, Megan Estorninho, Deborah Kronenberg-Versteeg, et al. 2014. "Blood and Islet Phenotypes Indicate Immunological Heterogeneity in Type 1 Diabetes." *Diabetes* 63 (11): 3835–45. https://doi.org/10.2337/db14-0365.

Bates, Douglas, Martin Mächler, Ben Bolker, and Steve Walker. 2015. "Fitting Linear Mixed-Effects Models Using Lme4." *Journal of Statistical Software* 67 (October): 1–48. https://doi.org/10.18637/jss.v067.i01.

Bender, Christine, Teresa Rodriguez-Calvo, Natalie Amirian, Ken T. Coppieters, and Matthias G. von Herrath. 2020. "The Healthy Exocrine Pancreas Contains Preproinsulin-Specific CD8 T Cells That Attack Islets in Type 1 Diabetes." *Science Advances* 6 (42): eabc5586. https://doi.org/10.1126/sciadv.abc5586.

Bhate, Salil S., Graham L. Barlow, Christian M. Schürch, and Garry P. Nolan. 2021. "Tissue Schematics Map the Specialization of Immune Tissue Motifs and Their Appropriation by Tumors." *Cell Systems*, October. https://doi.org/10.1016/j.cels.2021.09.012.

Black, Sarah, Darci Phillips, John W. Hickey, Julia Kennedy-Darling, Vishal G. Venkataraaman, Nikolay Samusik, Yury Goltsev, Christian M. Schürch, and Garry P. Nolan. 2021. "CODEX Multiplexed Tissue Imaging with DNA-Conjugated Antibodies." *Nature Protocols* 16 (8): 3802–35. https://doi.org/10.1038/s41596-021-00556-8.

Bluestone, Jeffrey A., Jane H. Buckner, and Kevan C. Herold. 2021. "Immunotherapy: Building a Bridge to a Cure for Type 1 Diabetes." *Science* 373 (6554): 510–16. https://doi.org/10.1126/science.abh1654.

Campbell-Thompson, Martha, Teresa Rodriguez-Calvo, and Manuela Battaglia. 2015. "Abnormalities of the Exocrine Pancreas in Type 1 Diabetes." *Current Diabetes Reports* 15 (10): 79. https://doi.org/10.1007/s11892-015-0653-y.

Campbell-Thompson, Martha, Clive Wasserfall, John Kaddis, Anastasia Albanese-O'Neill, Teodora Staeva, Concepcion Nierras, Jayne Moraski, et al. 2012. "Network for Pancreatic Organ Donors with Diabetes (NPOD): Developing a Tissue Biobank for Type 1 Diabetes." *Diabetes/Metabolism Research and Reviews* 28 (7): 608–17. https://doi.org/10.1002/dmrr.2316.

Castro-Gutierrez, Roberto, Aimon Alkanani, Clayton E. Mathews, Aaron Michels, and Holger A. Russ. 2021. "Protecting Stem Cell Derived Pancreatic Beta-Like Cells From Diabetogenic

T Cell Recognition." *Frontiers in Endocrinology* 12. https://www.frontiersin.org/articles/10.3389/fendo.2021.707881.

Christoffersson, Gustaf, Sowbarnika S. Ratliff, and Matthias G. von Herrath. 2020. "Interference with Pancreatic Sympathetic Signaling Halts the Onset of Diabetes in Mice." *Science Advances* 6 (35): eabb2878. https://doi.org/10.1126/sciadv.abb2878.

Dalmas, Elise, Frank M. Lehmann, Erez Dror, Stephan Wueest, Constanze Thienel, Marcela Borsigova, Marc Stawiski, et al. 2017. "Interleukin-33-Activated Islet-Resident Innate Lymphoid Cells Promote Insulin Secretion through Myeloid Cell Retinoic Acid Production." *Immunity* 47 (5): 928-942.e7. https://doi.org/10.1016/j.immuni.2017.10.015.

Damond, Nicolas, Stefanie Engler, Vito R. T. Zanotelli, Denis Schapiro, Clive H. Wasserfall, Irina Kusmartseva, Harry S. Nick, et al. 2019. "A Map of Human Type 1 Diabetes Progression by Imaging Mass Cytometry." *Cell Metabolism* 29 (3): 755-768.e5. https://doi.org/10.1016/j.cmet.2018.11.014.

Diggins, Kirsten E., Elisavet Serti, Virginia Muir, Mario Rosasco, TingTing Lu, Elisa Balmas, Gerald Nepom, S. Alice Long, and Peter S. Linsley. 2021. "Exhausted-like $CD8^+$ T Cell Phenotypes Linked to C-Peptide Preservation in Alefacept-Treated T1D Subjects." *JCI Insight* 6 (3). https://doi.org/10.1172/jci.insight.142680.

Fasolino, Maria, Gregory W. Schwartz, Abhijeet R. Patil, Aanchal Mongia, Maria L. Golson, Yue J. Wang, Ashleigh Morgan, et al. 2022. "Single-Cell Multi-Omics Analysis of Human Pancreatic Islets Reveals Novel Cellular States in Type 1 Diabetes." *Nature Metabolism* 4 (2): 284–99. https://doi.org/10.1038/s42255-022-00531-x.

Gelman, Andrew, John B Carlin, Hal S Stern, David B Dunson, Aki Vehtari, and Donald B Rubin. n.d. "Bayesian Data Analysis Third Edition (with Errors FIxed as of 15 February 2021)," 677.

Gepts, Willy. 1965. "Pathologic Anatomy of the Pancreas in Juvenile Diabetes Mellitus." *Diabetes* 14 (10): 619–33. https://doi.org/10.2337/diab.14.10.619.

Goltsev, Yury, Nikolay Samusik, Julia Kennedy-Darling, Salil Bhate, Matthew Hale, Gustavo Vazquez, Sarah Black, and Garry P. Nolan. 2018. "Deep Profiling of Mouse Splenic Architecture with CODEX Multiplexed Imaging." *Cell* 174 (4): 968-981.e15. https://doi.org/10.1016/j.cell.2018.07.010.

Gregory, Gabriel A., Thomas I. G. Robinson, Sarah E. Linklater, Fei Wang, Stephen Colagiuri, Carine de Beaufort, Kim C. Donaghue, et al. 2022. "Global Incidence, Prevalence, and Mortality of Type 1 Diabetes in 2021 with Projection to 2040: A Modelling Study." *The Lancet Diabetes & Endocrinology* 10 (10): 741–60. https://doi.org/10.1016/S2213-8587(22)00218-2.

Herold, Kevan C., Brian N. Bundy, S. Alice Long, Jeffrey A. Bluestone, Linda A. DiMeglio, Matthew J. Dufort, Stephen E. Gitelman, et al. 2019. "An Anti-CD3 Antibody, Teplizumab, in Relatives at Risk for Type 1 Diabetes." *New England Journal of Medicine* 381 (7): 603–13. https://doi.org/10.1056/NEJMoa1902226.

Herold, Kevan C., Stephen E. Gitelman, Mario R. Ehlers, Peter A. Gottlieb, Carla J. Greenbaum, William Hagopian, Karen D. Boyle, et al. 2013. "Teplizumab (Anti-CD3 MAb) Treatment Preserves C-Peptide Responses in Patients With New-Onset Type 1 Diabetes in a Randomized Controlled Trial: Metabolic and Immunologic Features at Baseline Identify a

Subgroup of Responders." *Diabetes* 62 (11): 3766–74. https://doi.org/10.2337/db13-0345.

Hickey, John W., Yuqi Tan, Garry P. Nolan, and Yury Goltsev. 2021. "Strategies for Accurate Cell Type Identification in CODEX Multiplexed Imaging Data." *Frontiers in Immunology* 12. https://www.frontiersin.org/article/10.3389/fimmu.2021.727626.

Hirsch, James S. 2023. "FDA Approves Teplizumab: A Milestone in Type 1 Diabetes." *The Lancet Diabetes & Endocrinology* 11 (1): 18. https://doi.org/10.1016/S2213-8587(22)00351-5.

In't Veld, Peter. 2011. "Insulitis in Human Type 1 Diabetes: The Quest for an Elusive Lesion." *Islets* 3 (4): 131–38. https://doi.org/10.4161/isl.3.4.15728.

Jerby-Arnon, Livnat, and Aviv Regev. 2022. "DIALOGUE Maps Multicellular Programs in Tissue from Single-Cell or Spatial Transcriptomics Data." *Nature Biotechnology* 40 (10): 1467–77. https://doi.org/10.1038/s41587-022-01288-0.

Kennedy-Darling, Julia, Salil S. Bhate, John W. Hickey, Sarah Black, Graham L. Barlow, Gustavo Vazquez, Vishal G. Venkataraaman, et al. 2021. "Highly Multiplexed Tissue Imaging Using Repeated Oligonucleotide Exchange Reaction." *European Journal of Immunology* 51 (5): 1262–77. https://doi.org/10.1002/eji.202048891.

Korpos, Éva, Nadir Kadri, Reinhild Kappelhoff, Jeannine Wegner, Christopher M. Overall, Ekkehard Weber, Dan Holmberg, Susanna Cardell, and Lydia Sorokin. 2013. "The Peri-Islet Basement Membrane, a Barrier to Infiltrating Leukocytes in Type 1 Diabetes in Mouse and Human." *Diabetes* 62 (2): 531–42. https://doi.org/10.2337/db12-0432.

Korpos, Éva, Nadir Kadri, Sophie Loismann, Clais R. Findeisen, Frank Arfuso, George W. Burke, Sarah J. Richardson, et al. 2021. "Identification and Characterisation of Tertiary Lymphoid Organs in Human Type 1 Diabetes." *Diabetologia* 64 (7): 1626–41. https://doi.org/10.1007/s00125-021-05453-z.

Krogvold, Lars, Bjørn Edwin, Trond Buanes, Johnny Ludvigsson, Olle Korsgren, Heikki Hyöty, Gun Frisk, Kristian F. Hanssen, and Knut Dahl-Jørgensen. 2014. "Pancreatic Biopsy by Minimal Tail Resection in Live Adult Patients at the Onset of Type 1 Diabetes: Experiences from the DiViD Study." *Diabetologia* 57 (4): 841–43. https://doi.org/10.1007/s00125-013-3155-y.

Kuric, Enida, Peter Seiron, Lars Krogvold, Bjørn Edwin, Trond Buanes, Kristian F. Hanssen, Oskar Skog, Knut Dahl-Jørgensen, and Olle Korsgren. 2017. "Demonstration of Tissue Resident Memory CD8 T Cells in Insulitic Lesions in Adult Patients with Recent-Onset Type 1 Diabetes." *The American Journal of Pathology* 187 (3): 581–88. https://doi.org/10.1016/j.ajpath.2016.11.002.

Kuznetsova, Alexandra, Per B. Brockhoff, and Rune H. B. Christensen. 2017. "LmerTest Package: Tests in Linear Mixed Effects Models." *Journal of Statistical Software* 82 (December): 1–26. https://doi.org/10.18637/jss.v082.i13.

Lee, Michael Y., Jacob S. Bedia, Salil S. Bhate, Graham L. Barlow, Darci Phillips, Wendy J. Fantl, Garry P. Nolan, and Christian M. Schürch. 2022. "CellSeg: A Robust, Pre-Trained Nucleus Segmentation and Pixel Quantification Software for Highly Multiplexed Fluorescence Images." *BMC Bioinformatics* 23 (1): 46. https://doi.org/10.1186/s12859-022-04570-9.

Leete, Pia, Abby Willcox, Lars Krogvold, Knut Dahl-Jørgensen, Alan K. Foulis, Sarah J. Richardson, and Noel G. Morgan. 2016. "Differential Insulitic Profiles Determine the Extent of β-Cell

925 Destruction and the Age at Onset of Type 1 Diabetes." *Diabetes* 65 (5): 1362–69.
926 https://doi.org/10.2337/db15-1615.
927 Martino, Luisa, Matilde Masini, Marco Bugliani, Lorella Marselli, Mara Suleiman, Ugo Boggi,
928 Tatiane C. Nogueira, et al. 2015. "Mast Cells Infiltrate Pancreatic Islets in Human Type 1
929 Diabetes." *Diabetologia* 58 (11): 2554–62. https://doi.org/10.1007/s00125-015-3734-1.
930 Munn, David H., and Andrew L. Mellor. 2016. "IDO in the Tumor Microenvironment:
931 Inflammation, Counter-Regulation, and Tolerance." *Trends in Immunology* 37 (3): 193–
932 207. https://doi.org/10.1016/j.it.2016.01.002.
933 Orban, Tihamer, Brian Bundy, Dorothy J. Becker, Linda A. DiMeglio, Stephen E. Gitelman, Robin
934 Goland, Peter A. Gottlieb, et al. 2011. "Co-Stimulation Modulation with Abatacept in
935 Patients with Recent-Onset Type 1 Diabetes: A Randomised, Double-Blind, Placebo-
936 Controlled Trial." *Lancet (London, England)* 378 (9789): 412–19.
937 https://doi.org/10.1016/S0140-6736(11)60886-6.
938 ———. 2014. "Costimulation Modulation With Abatacept in Patients With Recent-Onset Type 1
939 Diabetes: Follow-up 1 Year After Cessation of Treatment." *Diabetes Care* 37 (4): 1069–
940 75. https://doi.org/10.2337/dc13-0604.
941 Osum, Kevin C., Adam L. Burrack, Tijana Martinov, Nathanael L. Sahli, Jason S. Mitchell,
942 Christopher G. Tucker, Kristen E. Pauken, et al. 2018. "Interferon-Gamma Drives
943 Programmed Death-Ligand 1 Expression on Islet β Cells to Limit T Cell Function during
944 Autoimmune Diabetes." *Scientific Reports* 8 (1): 8295. https://doi.org/10.1038/s41598-
945 018-26471-9.
946 Penaranda, Cristina, Qizhi Tang, Nancy H. Ruddle, and Jeffrey A. Bluestone. 2010. "Prevention
947 of Diabetes by FTY720-Mediated Stabilization of Peri-Islet Tertiary Lymphoid Organs."
948 *Diabetes* 59 (6): 1461–68. https://doi.org/10.2337/db09-1129.
949 Perdigoto, Ana Luisa, Paula Preston-Hurlburt, Pamela Clark, S. Alice Long, Peter S. Linsley,
950 Kristina M. Harris, Steven E. Gitelman, et al. 2019. "Treatment of Type 1 Diabetes with
951 Teplizumab: Clinical and Immunological Follow-up after 7 Years from Diagnosis."
952 *Diabetologia* 62 (4): 655–64. https://doi.org/10.1007/s00125-018-4786-9.
953 Pescovitz, Mark D., Carla J. Greenbaum, Heidi Krause-Steinrauf, Dorothy J. Becker, Stephen E.
954 Gitelman, Robin Goland, Peter A. Gottlieb, et al. 2009. "Rituximab, B-Lymphocyte
955 Depletion, and Preservation of Beta-Cell Function." *New England Journal of Medicine*
956 361 (22): 2143–52. https://doi.org/10.1056/NEJMoa0904452.
957 Phillips, Darci, Magdalena Matusiak, Belén Rivero Gutierrez, Salil S. Bhate, Graham L. Barlow,
958 Sizun Jiang, Janos Demeter, et al. 2021. "Immune Cell Topography Predicts Response to
959 PD-1 Blockade in Cutaneous T Cell Lymphoma." *Nature Communications* 12 (1): 6726.
960 https://doi.org/10.1038/s41467-021-26974-6.
961 Phillips, Darci, Christian M. Schürch, Michael S. Khodadoust, Youn H. Kim, Garry P. Nolan, and
962 Sizun Jiang. 2021. "Highly Multiplexed Phenotyping of Immunoregulatory Proteins in the
963 Tumor Microenvironment by CODEX Tissue Imaging." *Frontiers in Immunology* 12:
964 687673. https://doi.org/10.3389/fimmu.2021.687673.
965 Pugliese, Alberto, Mingder Yang, Irina Kusmarteva, Tiffany Heiple, Francesco Vendrame, Clive
966 Wasserfall, Patrick Rowe, et al. 2014. "The Juvenile Diabetes Research Foundation
967 Network for Pancreatic Organ Donors with Diabetes (NPOD) Program: Goals,

968 Operational Model and Emerging Findings." *Pediatric Diabetes* 15 (1): 1–9.
969 https://doi.org/10.1111/pedi.12097.
970 Rodriguez-Calvo, Teresa, Olov Ekwall, Natalie Amirian, Jose Zapardiel-Gonzalo, and Matthias G.
971 von Herrath. 2014. "Increased Immune Cell Infiltration of the Exocrine Pancreas: A
972 Possible Contribution to the Pathogenesis of Type 1 Diabetes." *Diabetes* 63 (11): 3880–
973 90. https://doi.org/10.2337/db14-0549.
974 Rovituso, Damiano M., Laura Scheffler, Marie Wunsch, Christoph Kleinschnitz, Sebastian Dörck,
975 Jochen Ulzheimer, Antonios Bayas, Lawrence Steinman, Süleyman Ergün, and Stefanie
976 Kuerten. 2016. "CEACAM1 Mediates B Cell Aggregation in Central Nervous System
977 Autoimmunity." *Scientific Reports* 6 (July): 29847. https://doi.org/10.1038/srep29847.
978 Saelens, Wouter, Robrecht Cannoodt, Helena Todorov, and Yvan Saeys. 2019. "A Comparison of
979 Single-Cell Trajectory Inference Methods." *Nature Biotechnology* 37 (5): 547–54.
980 https://doi.org/10.1038/s41587-019-0071-9.
981 Sainburg, Tim, Leland McInnes, and Timothy Q. Gentner. 2021. "Parametric UMAP Embeddings
982 for Representation and Semi-Supervised Learning." arXiv.
983 https://doi.org/10.48550/arXiv.2009.12981.
984 Satpathy, Ansuman T., Jeffrey M. Granja, Kathryn E. Yost, Yanyan Qi, Francesca Meschi,
985 Geoffrey P. McDermott, Brett N. Olsen, et al. 2019. "Massively Parallel Single-Cell
986 Chromatin Landscapes of Human Immune Cell Development and Intratumoral T Cell
987 Exhaustion." *Nature Biotechnology* 37 (8): 925–36. https://doi.org/10.1038/s41587-019-
988 0206-z.
989 Savinov, Alexei Y., F. Susan Wong, Austin C. Stonebraker, and Alexander V. Chervonsky. 2003.
990 "Presentation of Antigen by Endothelial Cells and Chemoattraction Are Required for
991 Homing of Insulin-Specific CD8+ T Cells." *The Journal of Experimental Medicine* 197 (5):
992 643–56. https://doi.org/10.1084/jem.20021378.
993 Schürch, Christian M., Salil S. Bhate, Graham L. Barlow, Darci J. Phillips, Luca Noti, Inti Zlobec,
994 Pauline Chu, et al. 2020. "Coordinated Cellular Neighborhoods Orchestrate Antitumoral
995 Immunity at the Colorectal Cancer Invasive Front." *Cell*, August.
996 https://doi.org/10.1016/j.cell.2020.07.005.
997 Shekarian, Tala, Carl P. Zinner, Ewelina M. Bartoszek, Wandrille Duchemin, Anna T.
998 Wachnowicz, Sabrina Hogan, Manina M. Etter, et al. 2022. "Immunotherapy of
999 Glioblastoma Explants Induces Interferon-γ Responses and Spatial Immune Cell
1000 Rearrangements in Tumor Center, but Not Periphery." bioRxiv.
1001 https://doi.org/10.1101/2022.01.19.474897.
1002 Wang, Yue J., Daniel Traum, Jonathan Schug, Long Gao, Chengyang Liu, Mark A. Atkinson, Alvin
1003 C. Powers, et al. 2019. "Multiplexed In Situ Imaging Mass Cytometry Analysis of the
1004 Human Endocrine Pancreas and Immune System in Type 1 Diabetes." *Cell Metabolism*
1005 29 (3): 769-783.e4. https://doi.org/10.1016/j.cmet.2019.01.003.
1006 Wekerle, Hartmut. 2017. "B Cells in Multiple Sclerosis." *Autoimmunity* 50 (1): 57–60.
1007 https://doi.org/10.1080/08916934.2017.1281914.
1008 Wilcox, Nicholas S, Jinxiu Rui, Matthias Hebrok, and Kevan C Herold. 2016. "Life and Death of β
1009 Cells in Type 1 Diabetes: A Comprehensive Review." *Journal of Autoimmunity* 71 (July):
1010 51–58. https://doi.org/10.1016/j.jaut.2016.02.001.

Wolf, F. Alexander, Fiona K. Hamey, Mireya Plass, Jordi Solana, Joakim S. Dahlin, Berthold Göttgens, Nikolaus Rajewsky, Lukas Simon, and Fabian J. Theis. 2019. "PAGA: Graph Abstraction Reconciles Clustering with Trajectory Inference through a Topology Preserving Map of Single Cells." *Genome Biology* 20 (1): 59. https://doi.org/10.1186/s13059-019-1663-x.

Yi, Nengjun, Zaixiang Tang, Xinyan Zhang, and Boyi Guo. 2019. "BhGLM: Bayesian Hierarchical GLMs and Survival Models, with Applications to Genomics and Epidemiology." *Bioinformatics* 35 (8): 1419–21. https://doi.org/10.1093/bioinformatics/bty803.

Yoshihara, Eiji, Carolyn O'Connor, Emanuel Gasser, Zong Wei, Tae Gyu Oh, Tiffany W. Tseng, Dan Wang, et al. 2020. "Immune-Evasive Human Islet-like Organoids Ameliorate Diabetes." *Nature* 586 (7830): 606–11. https://doi.org/10.1038/s41586-020-2631-z.

Acknowledgements

This research was performed with the support of the Network for Pancreatic Organ donors with Diabetes (nPOD; RRID:SCR_014641), a collaborative type 1 diabetes research project supported by JDRF (nPOD: 5-SRA-2018-557-Q-R) and The Leona M. & Harry B. Helmsley Charitable Trust (Grant#2018PG-T1D053, G-2108-04793). The content and views expressed are the responsibility of the authors and do not necessarily reflect the official view of nPOD. Organ Procurement Organizations (OPO) partnering with nPOD to provide research resources are listed at http://www.jdrfnpod.org/for-partners/npod-partners/. Research reported in this publication was supported by the National Cancer Institute and National Institute of Allergy and Infectious Diseases of the National Institutes of Health under Award Numbers K99CA246061, 5U54CA209971-05, 5U2CCA233195-02, 1U2CCA233238-01, 5U2CCA233195-02, 5U01AI101984-09. The content is solely the responsibility of the authors and does not necessarily represent the official views of the National Institutes of Health. C.M.S. was supported by the Swiss National Science Foundation (P300PB_171189, P400PM_183915). We like to thank Yury Goltsev, Pauline Chu, Sarah Black, Gustavo Vazquez, Aviv Hargil (Stanford University), and Irina Kusmartseva (nPOD) for excellent assistance. We like to thank Dr. Xavier Rovira-Clavé (Stanford University) for critical comments on the manuscript.

Author information

G.L.B curated data, wrote software, and analyzed data. D.P. and C.M.S contributed significantly to validating the antibody panel and assisted with analysis. S.D., S.S.B, A.Y., H.A.M., G.K.K., N.N., S.R., and J.M. assisted with analysis. G.L.B., J.A.B., G.P.N., and P.L.B., conceptualized the study and wrote the manuscript. All authors have read and approved the final version of the manuscript.

Ethics declarations

P.L.B.: Founder, Halo Biosciences.

N.N.: Founder, Halo Biosciences.

PLB, NN and GK have filed intellectual property around 4-MU. PLB, NN and GK hold a financial interest in Halo Biosciences, a company that is developing 4-MU for various indications.

G.P.N. has received research grants from Vaxart and Celgene during the course of this work and has equity in and is a scientific advisory board member of Akoya Biosciences. Akoya Biosciences makes reagents and instruments that are dependent on licenses from Stanford University. Stanford University has been granted US patent 9909167, which covers some aspects of the technology described in this paper.

J.A.B.: Board of director for Gilead and CEO and President of Sonoma Biotherapeutics; scientific advisory boards of Arcus Biotherapeutics and Cimeio Therapeutics; consultant for Rheos Medicines, Provention Bio; stockholder in Rheos Medicines, Vir Therapeutics, Arcus Biotherapeutics, Solid Biosciences, Celsius Therapeutics; Gilead Sciences, Provention Bio, Sonoma Biotherapeutics.

C.M.S.: Scientific advisory board of, stock options in, research funding from Enable Medicine, Inc.